

CD4⁺ T cell-induced inflammatory cell death controls immune-evasive tumours


<https://doi.org/10.1038/s41586-023-06199-x>

Received: 16 June 2022

Accepted: 11 May 2023

Published online: 14 June 2023

Open access

 Check for updates

Bastian Kruse^{1,15}, Anthony C. Buzzai^{1,15}, Naveen Shridhar^{1,15}, Andreas D. Braun^{1,15}, Susan Gellert¹, Kristin Knauth¹, Joanna Pozniak^{2,3}, Johannes Peters¹, Paulina Dittmann¹, Miriam Mengoni¹, Tetje Cornelia van der Sluis¹, Simon Höhn¹, Asier Antoranz⁴, Anna Krone⁵, Yan Fu⁵, Di Yu⁶, Magnus Essand⁶, Robert Geffers⁷, Dimitrios Mouggiakakos⁸, Sascha Kahlfuß⁵, Hamid Kashkar⁹, Evelyn Gaffal¹, Francesca M. Bosisio¹⁰, Oliver Bechter¹¹, Florian Rambow^{12,13}, Jean-Christophe Marine^{2,3}, Wolfgang Kastenmüller¹⁴, Andreas J. Müller^{5,16}✉ & Thomas Tüting^{1,16}✉

Most clinically applied cancer immunotherapies rely on the ability of CD8⁺ cytolytic T cells to directly recognize and kill tumour cells^{1–3}. These strategies are limited by the emergence of major histocompatibility complex (MHC)-deficient tumour cells and the formation of an immunosuppressive tumour microenvironment^{4–6}. The ability of CD4⁺ effector cells to contribute to antitumour immunity independently of CD8⁺ T cells is increasingly recognized, but strategies to unleash their full potential remain to be identified^{7–10}. Here, we describe a mechanism whereby a small number of CD4⁺ T cells is sufficient to eradicate MHC-deficient tumours that escape direct CD8⁺ T cell targeting. The CD4⁺ effector T cells preferentially cluster at tumour invasive margins where they interact with MHC-II⁺CD11c⁺ antigen-presenting cells. We show that T helper type 1 cell-directed CD4⁺ T cells and innate immune stimulation reprogramme the tumour-associated myeloid cell network towards interferon-activated antigen-presenting and iNOS-expressing tumouricidal effector phenotypes. Together, CD4⁺ T cells and tumouricidal myeloid cells orchestrate the induction of remote inflammatory cell death that indirectly eradicates interferon-unresponsive and MHC-deficient tumours. These results warrant the clinical exploitation of this ability of CD4⁺ T cells and innate immune stimulators in a strategy to complement the direct cytolytic activity of CD8⁺ T cells and natural killer cells and advance cancer immunotherapies.

Adoptive cell transfer (ACT) studies using tumour-infiltrating lymphocytes from patients that are expanded *ex vivo* before their reinfusion provided initial proof-of-principle for the clinical efficacy of T cell immunotherapy¹¹. The recent success of the immune checkpoint blockade (ICB) with monoclonal antibodies targeting the immunoregulatory receptors CTLA4 and PD1 led to the clinical breakthrough of T cell-directed immunotherapies¹². The efficacy of ICB is mainly attributed to reactivation of CD8⁺ T cells that specifically recognize tumour antigens in the form of processed peptide epitopes presented by major histocompatibility complex class I (MHC-I) molecules on tumour cells. Both antigen presentation and MHC expression are upregulated by interferons (IFNs). Following antigen recognition, CD8⁺ T cells release cytolytic granules and IFN γ

that initiate cell death. Despite its clinical efficacy, ICB is limited by the emergence of MHC-deficient and IFN-unresponsive tumour cell clones that escape recognition and destruction by CD8⁺ cytolytic T cells^{4,5}.

There is emerging evidence that CD4⁺ T cells can also contribute to antitumour immunity, independent of their role as helpers and regulators of CD8⁺ cytolytic T cells¹³. A subset of CD4⁺ T cells develops cytolytic effector functions towards MHC-II-expressing tumour cells^{14,15}. In addition, CD4⁺ T cells were shown capable of eradicating tumour cells that do not express MHC-II by mobilizing myeloid cells, which are specialized to process and present peptide epitopes on their MHC-II molecules^{16–18}. The therapeutic potential of this indirect CD4⁺ T cell effector mechanism has, however, remained unclear. Moreover, the

¹Laboratory of Experimental Dermatology, Department of Dermatology, University Hospital and Health Campus Immunology Infectiology and Inflammation (GC-I3), Otto-von-Guericke University, Magdeburg, Germany. ²Laboratory for Molecular Cancer Biology, Center for Cancer Biology, VIB, Leuven, Belgium. ³Laboratory for Molecular Cancer Biology, Department of Oncology, KU Leuven, Leuven, Belgium. ⁴Translational Cell and Tissue Research, Department of Imaging and Pathology, KU Leuven, Leuven, Belgium. ⁵Institute of Molecular and Clinical Immunology, Health Campus Immunology Infectiology and Inflammation (GC-I3), Otto-von-Guericke University, Magdeburg, Germany. ⁶Department of Immunology, Genetics and Pathology, Uppsala University, Uppsala, Sweden. ⁷Helmholtz Centre for Infection Research, Brunswick, Germany. ⁸Department of Hematology, University Hospital and Health Campus Immunology Infectiology and Inflammation (GC-I3), Otto-von-Guericke University, Magdeburg, Germany. ⁹Institute for Molecular Immunology, Centre for Molecular Medicine Cologne and Cologne Excellence Cluster on Cellular Stress Responses in Ageing-Associated Diseases, University of Cologne, Cologne, Germany. ¹⁰Department of Pathology, UZ Leuven, Leuven, Belgium. ¹¹Department of General Medical Oncology, UZ Leuven, Leuven, Belgium. ¹²Department of Applied Computational Cancer Research, Institute for AI in Medicine (IKIM), University Hospital Essen, Essen, Germany. ¹³University of Duisburg-Essen, Essen, Germany. ¹⁴Institute for Systems Immunology, Wuerzburg, Germany. ¹⁵These authors contributed equally: Bastian Kruse, Anthony Buzzai, Naveen Shridhar, Andreas Braun. ¹⁶These authors jointly supervised this work: Andreas J. Müller, Thomas Tüting. ✉e-mail: andreas.mueller@med.ovgu.de; thomas.tueing@med.ovgu.de

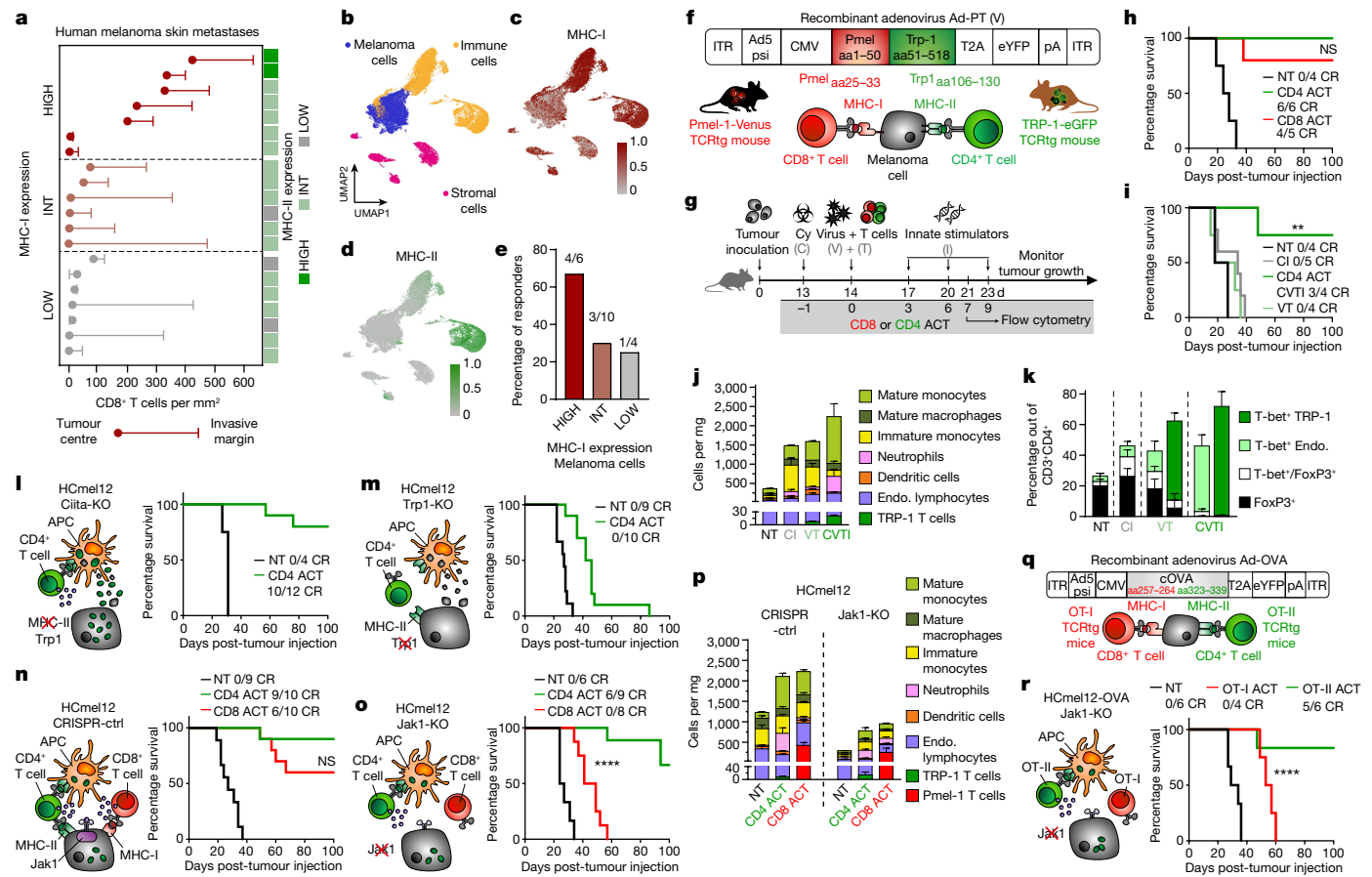


Fig. 1 | A small population of CD4⁺ effector T cells can eradicate MHC-deficient and IFN-unresponsive melanomas that resist destruction by CD8⁺ cytotoxic T cells. **a**, Density of CD8⁺ T cells infiltrating the tumour centre and the invasive margin of 20 human melanoma skin metastases and corresponding MHC-I and MHC-II expression, categorized into high, intermediate (int) and low expression. **b**, UMAP of single-cell transcriptomes from an extra set of 20 melanoma metastases in skin ($n = 5$), subcutis ($n = 4$) and lymph nodes ($n = 11$) annotated for melanoma, immune and stromal cell phenotypes. **c, d**, MHC-I (**c**) and MHC-II (**d**) gene set expression in single melanoma cells. **e**, ICB therapy responders in patients with high, intermediate and low MHC-I expression on melanoma cells. **f**, Structure of recombinant adenovirus Ad-PT. **g**, Experimental protocol for ACT immunotherapy of established Trp1 melanomas in mice (Cy, C, cyclophosphamide; V, Ad-PT; T, TCRtg Pmel-1 CD8⁺ or TRP-1 CD4⁺ T cells; I, innate stimuli, polyI:C and CpG) and time point for flow cytometric analyses. **h, i**, Kaplan–Meier survival curves of mice bearing established B16 melanomas and treated either with CD4 ACT or CD8 ACT (**h**) or with the indicated

components of the CD4 ACT protocol (**i**). NT, non-treated; CR, complete responders. **i**, $^{**}P = 0.0084$. **j, k**, Immune cell composition ($n = 2$ biologically independent samples) (**j**) and phenotype of endogenous and transferred (VT, CVTI, right columns) CD4⁺ T cells (**k**) in tumours treated as indicated (mean \pm s.e.m. from $n = 4$ biologically independent samples). **l–o**, Graphical representation of the immune cell interaction phenotypes (left) and Kaplan–Meier survival curves (right) of mice bearing established Ciita-KO (**l**), Trp1-KO (**m**), CRISPR-ctrl (**n**) or Jak1-KO (**o**) melanomas and treated as indicated. **o**, $^{****}P < 0.0001$. **p**, Immune cell composition of tumours treated as indicated (mean \pm s.e.m. from four biologically independent samples). **q**, Structure of recombinant adenovirus Ad-OVA. **r**, Graphical representation of the immune cell interaction phenotype of ovalbumin-expressing Hcmel12 Jak1-KO cells (left) and Kaplan–Meier survival curves (right) of mice bearing established melanomas treated as indicated. $^{****}P < 0.0001$. Survival was statistically compared using a log-rank Mantel–Cox test. NS, not significant.

spatiotemporal dynamics and the mechanism of action of CD4⁺ T cells within the tumour tissue have not been fully explained.

Clinical relevance of immune evasion

Tumour cells can evade recognition and destruction by CD8⁺ T cells through MHC-I downregulation¹⁹. We reassessed the clinical relevance of this immune evasion mechanism in skin metastases of patients with melanoma by immunohistochemistry. Our results show very low MHC-I expression on melanoma cells in seven out of 20 samples that was associated with the absence of tumour-infiltrating CD8⁺ T cells (Fig. 1a and Extended Data Fig. 1a, b). Expression of MHC-II was mostly restricted to stromal and immune cells at the invasive margins in 15 out of 20 samples, often in association with infiltrating CD8⁺ T cells. Only two out of 20 samples that were densely infiltrated with CD8⁺ T cells showed high

expression levels of MHC-II on melanoma cells, whereas three out of 20 samples that lacked CD8⁺ T cell infiltrates barely expressed MHC-II (Fig. 1a and Extended Data Fig. 1c).

We independently analysed the expression of MHC molecules in single-cell RNA-sequencing (scRNA-seq) data obtained from a different cohort of 20 patients with treatment-naïve melanoma metastases (Fig. 1b–e)²⁰. Transcriptional MHC-I downregulation in melanoma cells was evident in four out of 20 samples (Fig. 1c and Extended Data Fig. 1d). MHC-II expression was largely absent in melanoma cells and restricted to antigen-presenting immune cells (Fig. 1d and Extended Data Fig. 1e–g). Transcriptional downregulation of MHC-I on melanoma cells was associated with poor response to ICB (Fig. 1e). In aggregate, these results indicate that MHC-I downregulation in tumour cells is a frequent phenomenon during tumour evolution that favours immune escape.

Establishment of a CD4 ACT model

To experimentally investigate how CD4⁺ T cell effector functions could be therapeutically directed against MHC-deficient tumours that evade CD8⁺ T cell immunity, we used enhanced green fluorescent protein (eGFP⁺) TRP-1 CD4⁺ TCRtg T cells and Venus⁺ Pmel-1 CD8⁺ TCRtg T cells for ACT immunotherapies^{21,22}. Vaccination with the recombinant adenovirus Ad-PT encoding a Pmel/gp100-TRP-1 fusion protein capable of stimulating both CD4⁺ and CD8⁺ TCRtg T cells (Fig. 1f) allowed us to directly compare their antitumour efficacy and their mechanism of action under identical experimental conditions using the ACT therapy protocol established in our previous work²³ (Fig. 1g). This protocol includes chemotherapeutic preconditioning with cyclophosphamide, a procedure also used in clinical ACT approaches, and adjuvant injections of the immunostimulatory oligonucleotides poly:I:C and CpG that activate innate immunity through TLR3 and TLR9, respectively²⁴. Similar oligonucleotides are currently explored in early phase clinical trials^{25,26}.

Initial experiments demonstrated that adoptively transferred TRP-1 CD4⁺ T cells expanded much less efficiently in lymph nodes, peripheral blood and spleens when compared with adoptively transferred Pmel-1 CD8⁺ T cells (Extended Data Fig. 2a,b). This observation is in line with the previously described intrinsic difference in the proliferative capacity between CD4⁺ and CD8⁺ T cells²⁷. Despite their relatively poor *in vivo* expansion, adoptively transferred TRP-1 CD4⁺ T cells eradicated established B16 melanomas as efficiently as Pmel-1 CD8⁺ T cells (Fig. 1h and Extended Data Fig. 2c,d).

Cyclophosphamide pretreatment and innate immune stimulation were required in our CD4 ACT protocol to eradicate established tumours (Fig. 1i and Extended Data Fig. 2e,f), similar to our findings for CD8 ACT²⁴. Flow cytometric analyses of tumour-infiltrating CD4⁺ cells at day 7 after adoptive T cell transfer revealed a comparatively small subpopulation of adoptively transferred TRP-1 CD4⁺ T cells representing only 1% of immune cells in treated mice (Fig. 1j and Extended Data Fig. 2g,h). The combination of cyclophosphamide pretreatment and adjuvant innate immune stimulation strongly promoted the differentiation of transferred and endogenous CD4⁺ T cells towards a T helper (T_H) type 1 (T_H1)-directed phenotype and prevented the accumulation of regulatory T cells (Fig. 1k and Extended Data Fig. 2i). The adoptive transfer of T cells and the injection of innate immune stimuli independently increased the myeloid immune infiltrate that consisted predominantly of monocytes and macrophages. The full ACT protocol further increased the accumulation of monocytes (Fig. 1j).

Indirect tumour recognition

TRP-1 CD4⁺ T cells can eradicate B16 melanomas through direct recognition and cytolytic destruction¹⁴. However, most human melanoma cells do not express MHC-II molecules¹⁰ (Extended Data Fig. 1c,e). We therefore investigated the ability of TRP-1 CD4⁺ T cells to control MHC-II-deficient tumour cells by disrupting the *Ciita* gene encoding the MHC-II transactivator in Hcmel12 mouse melanoma cells using CRISPR-Cas9 gene editing (Extended Data Fig. 2j). As controls, we also generated Hcmel12 Trp1-knockout (Trp1-KO) cells that lack expression of the CD4⁺ T cell target antigen (Extended Data Fig. 2k). *In vitro* experiments confirmed that TRP-1 CD4⁺ T cells can directly respond to MHC-II-expressing Hcmel12 cells in an antigen-specific manner (Extended Data Fig. 2l), but are more efficiently activated indirectly by MHC-II+ dendritic cells pulsed with Hcmel12 cell lysates (Extended Data Fig. 2m). Of note, 40% of TRP-1 CD4⁺ T cells isolated from CD4 ACT-treated mice produced IFN γ following stimulation with tumour lysate-pulsed dendritic cells, confirming their T_H1 phenotype.

Subsequent *in vivo* experiments showed that TRP-1 CD4⁺ T cells were able to eradicate established MHC-II-deficient, but not TRP-1-deficient Hcmel12 melanomas (Fig. 1l,m and Extended Data Fig. 2n-p). Treatment of tumours consisting of Hcmel12 CRISPR-control (ctrl) and

Hcmel12 Trp1-KO mixtures demonstrated that TRP-1 CD4⁺ T cells also exerted substantial bystander killing activity, but could not prevent the outgrowth of Hcmel12 Trp1-KO cells in all mice (Extended Data Fig. 2q,r). Furthermore, antibody-mediated depletion experiments confirmed that the treatment efficacy of TRP-1 CD4⁺ T cells did not require the presence of CD8⁺ T cells (Extended Data Fig. 2s,t). Thus, TRP-1 CD4⁺ T cells can indirectly recognize and kill MHC-II-deficient tumour cells in the absence of CD8⁺ T cells.

Eradication of immune-evasive tumours

In subsequent experiments, we took advantage of the unique properties of Hcmel12 melanoma cells that constitutively lack MHC-I and MHC-II expression unless exposed to IFNs. CRISPR-Cas9-mediated disruption of the *Jak1* gene encoding for a central mediator of the IFN signalling pathway leads to IFN-unresponsive and completely MHC-deficient tumour cells (Extended Data Fig. 3a). Robust *in vivo* growth of Hcmel12 *Jak1*-KO melanoma cells required antibody-mediated depletion of natural killer (NK) cells before tumour inoculation, in line with the known ability of NK cells to directly recognize and kill MHC-I-deficient cells by cytotoxicity. This experimental setting allowed us to investigate the capacity of adoptively transferred TRP-1 CD4⁺ T cells to indirectly recognize and kill IFN-unresponsive, MHC-deficient tumour cells independent from their ability to directly target and lyse MHC-II-expressing tumour cells and to provide help for the cytotoxic activity of CD8⁺ T and NK cells. Our results demonstrate that adoptively transferred TRP-1 CD4⁺ T cells can indirectly eradicate established tumours that evade CD8⁺ T cell control in the absence of NK cells (Fig. 1n,o and Extended Data Fig. 3b,c).

Subsequent flow cytometric analyses revealed that adoptively transferred Pmel-1 CD8⁺ T cells represented a much larger subpopulation of tumour-infiltrating immune cells when compared to adoptively transferred TRP-1 CD4⁺ T cells, both in Hcmel12 CRISPR-ctrl and Hcmel12 *Jak1*-KO tumours, consistent with their differential *in vivo* expansion dynamics. Nevertheless, both CD4 and CD8 ACT therapies substantially increased the number of myeloid cells in Hcmel12 CRISPR-ctrl and Hcmel12 *Jak1*-KO tumours (Fig. 1p and Extended Data Fig. 3d,e). The increased immune cell infiltrate was less pronounced in MHC-deficient Hcmel12 *Jak1*-KO tumours when compared to Hcmel12 CRISPR-ctrl tumours, in line with our observation in patient samples (Fig. 1a and Extended Data Fig. 1a,b).

Using ovalbumin as a second tumour antigen model (Fig. 1q), we recapitulated the different *in vivo* expansion dynamics of adoptively transferred ovalbumin-specific OT-II TCRtg CD4⁺ T cells and OT-I TCRtg CD8⁺ T cells (Extended Data Fig. 3f,g). Again, ovalbumin-specific OT-II TCRtg CD4⁺ T cells were able to eradicate ovalbumin-expressing MHC-deficient Hcmel12 *Jak1*-KO tumours, whereas ovalbumin-specific OT-I TCRtg CD8⁺ T cells were ineffective (Fig. 1r and Extended Data Fig. 3h,i). Taken together, these results confirmed that a few CD4⁺ effector T cells can indirectly eradicate established IFN-unresponsive, MHC-deficient tumours that evade CD8⁺ T cell immunity independent of NK cells.

Intratumoural CD4⁺ T cell dynamics

We proposed that CD4⁺ effector T cells are efficiently activated in tumour tissues by antigen-presenting immune cells that constitutively express MHC-II, whereas CD8⁺ T cells require MHC-I-restricted antigen presentation by tumour cells. The expression pattern of MHC molecules in tumour tissues should therefore also determine the spatial distribution and migratory behaviour of adoptively transferred CD4⁺ and CD8⁺ T cells. To address these hypotheses, we generated amelanotic (Tyr-KO) Hcmel12 CRISPR-ctrl and Hcmel12 *Jak1*-KO cells that express tag-blue fluorescent protein (tagBFP) for immunofluorescence microscopy imaging (Extended Data Fig. 4a). Confocal microscopy showed only very few adoptively transferred eGFP⁺ TRP-1 CD4⁺ T cells in local clusters at the invasive margin of established amelanotic tagBFP-labelled

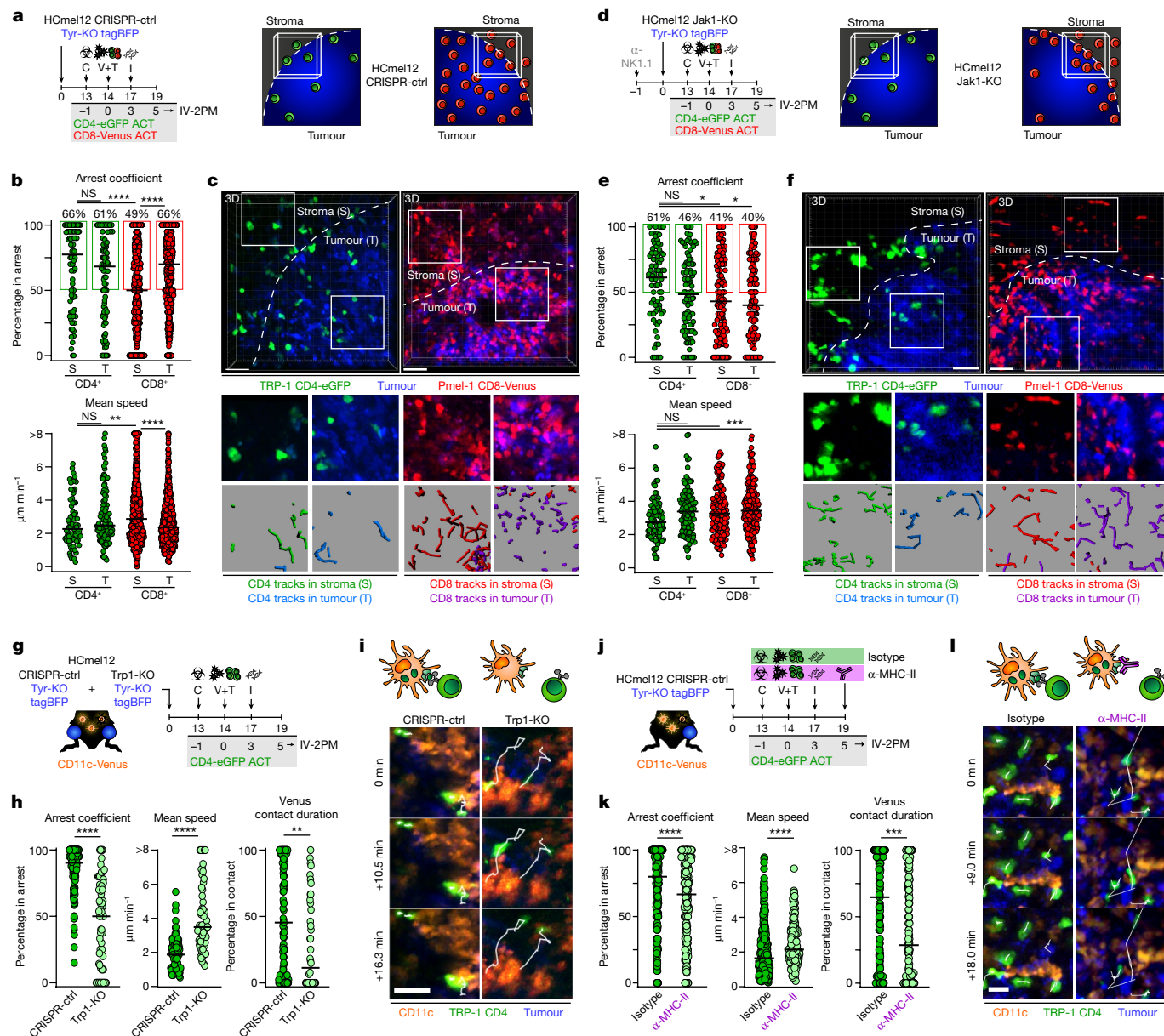


Fig. 2 | CD4⁺ effector T cells interact with MHC-II-expressing CD11c⁺ antigen-presenting cells in clusters within the invasive tumour margin. **a,d**, Experimental protocols to assess the distribution of adoptively transferred T cells (left) and graphics depicting the invasive tumour margin (right) of CRISPR-ctrl (**a**) or Jak1-KO (**d**) tumours. **b,e**, Arrest coefficient and mean speed of adoptively transferred Venus⁺ Pmel-1 CD8⁺ (red) and eGFP⁺ TRP-1 CD4⁺ T cells (green) in the stromal (S) and tumoural (T) compartment at the invasive margin (bars indicate the median) of CRISPR-ctrl (**b**) or Jak1-KO (**e**) tumours (75–842 cells examined from three independent experiments; *****P* < 0.0001, ****P* = 0.0007, ***P* = 0.0068, CD4⁺ versus CD8⁺ in stroma **P* = 0.0204, CD4⁺ in stroma versus CD8⁺ in tumour **P* = 0.0107 using a Kruskal–Wallis test with Dunn’s multiple comparison test). **c,f**, Representative intravital microscopic images (scale bars, 100 μm) and insets exemplifying 450 s motion tracks of Venus⁺ Pmel-1 CD8⁺ and eGFP⁺ TRP-1 CD4⁺ T cells at the stromal (S) and tumoural (T) area of the invasive tumour margin of CRISPR-ctrl (**c**) or Jak1-KO (**f**) melanomas. **g**, Experimental protocol to assess antigen-dependent interactions between eGFP⁺ TRP-1 CD4⁺

T cells and CD11c⁺ immune cells. **h**, Arrest coefficient, mean speed and relative contact duration between eGFP⁺ TRP-1 CD4⁺ T cells and CD11c-Venus cells (the bars indicate the median; 43–132 cells examined from three independent experiments; *****P* < 0.0001, ***P* = 0.0022 with a Mann–Whitney *U*-test). **i**, Representative motion tracks of eGFP⁺ TRP-1 CD4⁺ T cells interacting with CD11c-Venus cells in CRISPR-ctrl and Trp1-KO melanomas. Scale bars, 20 μm. **j**, Experimental protocol to assess the impact of MHC-II blockade on antigen-dependent interactions between eGFP⁺ TRP-1 CD4⁺ T cells and CD11c⁺ immune cells. **k**, Arrest coefficient, mean speed and relative contact duration between eGFP⁺ TRP-1 CD4⁺ T cells and CD11c-Venus cells (the bars indicate the median; 203–273 cells examined from three independent experiments; *****P* < 0.0001, ****P* = 0.0003, with a Mann–Whitney *U*-test). **l**, Representative motion tracks of eGFP⁺ TRP-1 CD4⁺ T cells interacting with CD11c-Venus cells in CRISPR-ctrl Tyr-KO tumours with and without MHC-II blockade. Scale bars, 20 μm. Data were pooled from at least three independent mice and groups statistically compared using a one-way ANOVA with Tukey post hoc.

HCmel12 CRISPR-ctrl tumours. By contrast, large numbers of Venus⁺ Pmel-1 CD8⁺ T cells infiltrated both the invasive margin and the tumour centre (Extended Data Fig. 4b,d), consistent with the flow cytometry results (Fig. 1j,p). TRP-1 CD4⁺ T cells also locally clustered at the invasive

margin of MHC-deficient HCmel12 Jak1-KO tumours, whereas Pmel-1 CD8⁺ T cells only infiltrated the invasive margin but not the tumour centre (Extended Data Fig. 4c,e). These results showed that the distribution of CD8⁺ T cells in tumour tissues of our preclinical model depends

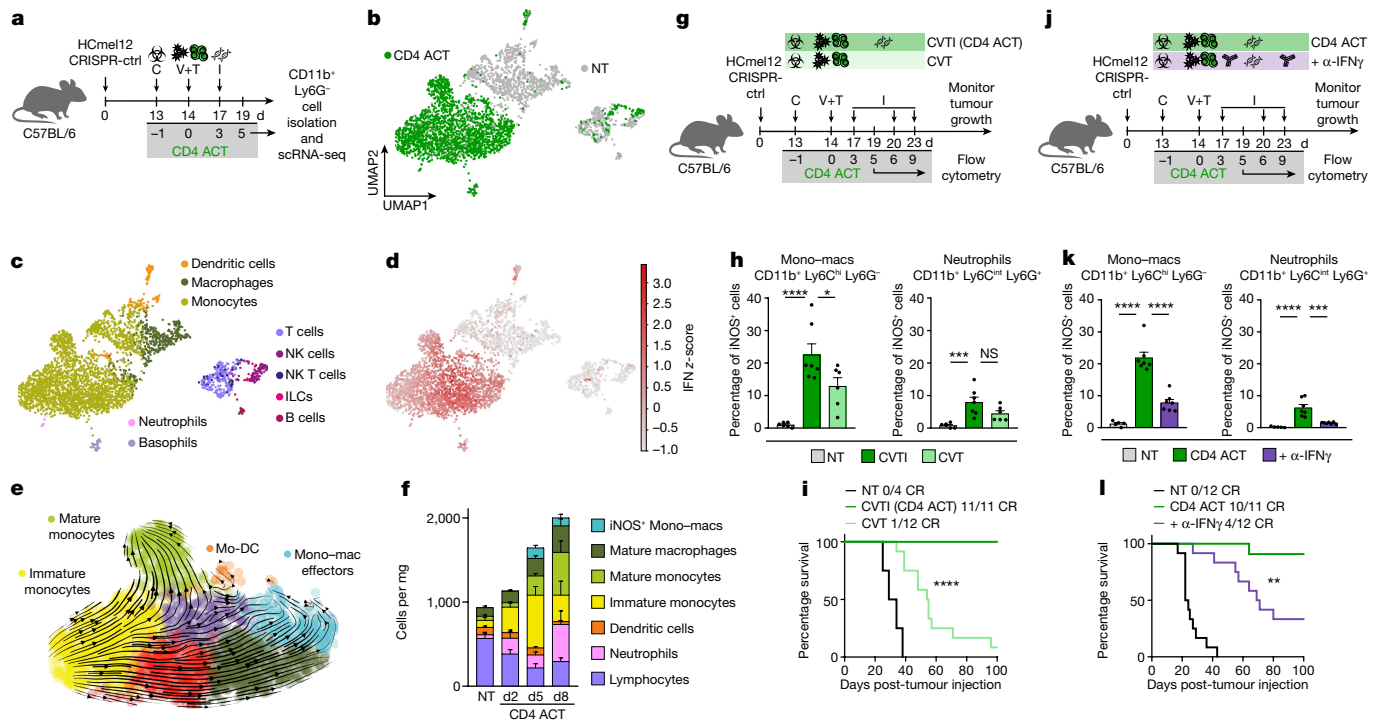


Fig. 3 | CD4⁺ effector T cells and innate immune stimulation promote the recruitment and IFN-dependent activation of monocytes to eradicate established tumours. **a**, Experimental protocol for scRNA-seq analyses of tumour-infiltrating CD11b⁺ Ly6G⁻ cells. **b**, Visualization and dimensionality reduction of single-cell transcriptomes from CD4 ACT-treated and non-treated (NT) mice using UMAP. **c**, UMAP plots with cell types assigned using SingleR (**c**) and z-score for the hallmark IFN gamma response gene set (MSigDB) of each cell (**d**). **e**, RNA velocity projected on UMAP plots for monocytes and macrophages (Mono-macs) of CD4 ACT-treated tumours. Arrows point towards the predicted course of cell maturation dynamics. Arrow sizes indicate the strength of predicted directionality. **f**, Immune cell composition of HCmel12 tumours treated as indicated (mean ± s.e.m. from *n* = 6 biologically

independent samples). **g**, **j**, Experimental treatment protocol to investigate the impact of innate stimuli (**g**) or IFN- γ blockade (**j**) on myeloid cell activation and tumour control. **h**, **k**, Percentage of intratumoural iNOS⁺ mono-macs and neutrophils (mean ± s.e.m. from *n* = 5–7 biologically independent samples). **h**, *****P* < 0.0001, **P* = 0.0111, ****P* = 0.0005; **k**, *****P* < 0.0001, ****P* = 0.0002). **i**, **l**, Kaplan–Meier survival curves of mice bearing established HCmel12 CRISPR-ctrl tumours, treated as indicated (**i**, *****P* < 0.0001; **l**, ***P* = 0.0053). Means between groups were statistically compared using a one-way ANOVA with Tukey post hoc. Survival was statistically compared using log-rank Mantel–Cox test. NT, non-treated; C, cyclophosphamide; V, Ad-PT; T, TCRtg TRP-1 CD4⁺ T cells; I, innate stimuli, polyI:C and CpG; CR, complete responders.

on MHC-I expression, reminiscent of the spatial distribution of CD8⁺ T cells in human melanomas (Extended Data Fig. 1b).

Intravital two-photon microscopy at the invasive margin confirmed the differential intratumoural localization of adoptively transferred CD4⁺ and CD8⁺ T cells and revealed substantial differences in their migratory behaviour. In HCmel12 CRISPR-ctrl tumours, CD4⁺ T cells arrested both in the stromal and the tumoural compartment within the invasive margin, whereas CD8⁺ T cells remained highly motile in the stroma and only arrested in the tumoural compartment (Fig. 2a–c and Supplementary Videos 1 and 2). In MHC-deficient HCmel12 Jak1-KO tumours, CD4⁺ T cells showed no changes in their migratory behaviour in the stroma and a slightly increased motility in the tumoural compartment of the invasive margin. By contrast, CD8⁺ T cells failed to arrest at all and were always highly motile in MHC-deficient HCmel12 Jak1-KO melanomas (Fig. 2d–f and Supplementary Videos 3 and 4). Together, these observations indicated that CD4⁺ T cells can interact with MHC-II⁺ immune and tumour cells at the invasive margin, whereas CD8⁺ T cells predominantly interact with MHC-I⁺ tumour cells.

We confirmed the fundamental difference in the spatial distribution and migratory behaviour of CD4⁺ and CD8⁺ T cells in tumour tissues using amelanotic (Tyr-KO) MHC-deficient HCmel12 Jak1-KO tumours that express tagBFP-Ova. Very few adoptively transferred ovalbumin-specific dsRed⁺ OT-II CD4⁺ TCRtg T cells clustered locally within the tumour invasive margin and arrested both in the stromal and the tumoural compartment. By contrast, large numbers of ovalbumin-specific Venus⁺ OT-I CD8⁺ TCRtg T cells infiltrated only the

tumour invasive margin but not the tumour centre and were always highly motile (Extended Data Fig. 4f,g). These observations confirmed that CD4⁺ T cells preferentially interact with MHC-II⁺ antigen-presenting cells at the invasive tumour margin, whereas CD8⁺ T cells require MHC-I expression on tumour cells to exert their effector functions in vivo.

MHC-II-restricted antigen recognition

A likely interaction partner for CD4⁺ T cells are dendritic cells due to their ability to efficiently ingest and process tumour antigens for MHC-II-dependent antigen presentation^{28–30}. To visualize antigen-specific interactions between TRP-1 CD4⁺ T cells and MHC-II⁺ CD11c⁺ antigen-presenting cells, we further generated amelanotic (Tyr-KO) HCmel12 Trp1-KO cells expressing tagBFP, injected them into opposite legs of CD11c-Venus transgenic mice that harbour fluorescent antigen-presenting immune cells³¹ and treated established tumours with adoptively transferred eGFP⁺ TRP-1 CD4⁺ T cells (Fig. 2g and Extended Data Fig. 5a,b). Confocal microscopy revealed local accumulations of eGFP⁺ TRP-1 CD4⁺ T cells in association with MHC-II-expressing CD11c-Venus⁺ immune cells within tumour invasive margins in HCmel12 CRISPR-ctrl but not in HCmel12 Trp1-KO tumours (Extended Data Fig. 5c–f). Tumour cells surrounding clusters of CD11c-Venus⁺ immune cells with CD4⁺ T cells upregulated the expression of MHC-II exclusively in mice bearing HCmel12 CRISPR-ctrl tumours, consistent with the notion that CD4⁺ T cells were activated locally and secreted IFN- γ in an antigen-dependent manner.

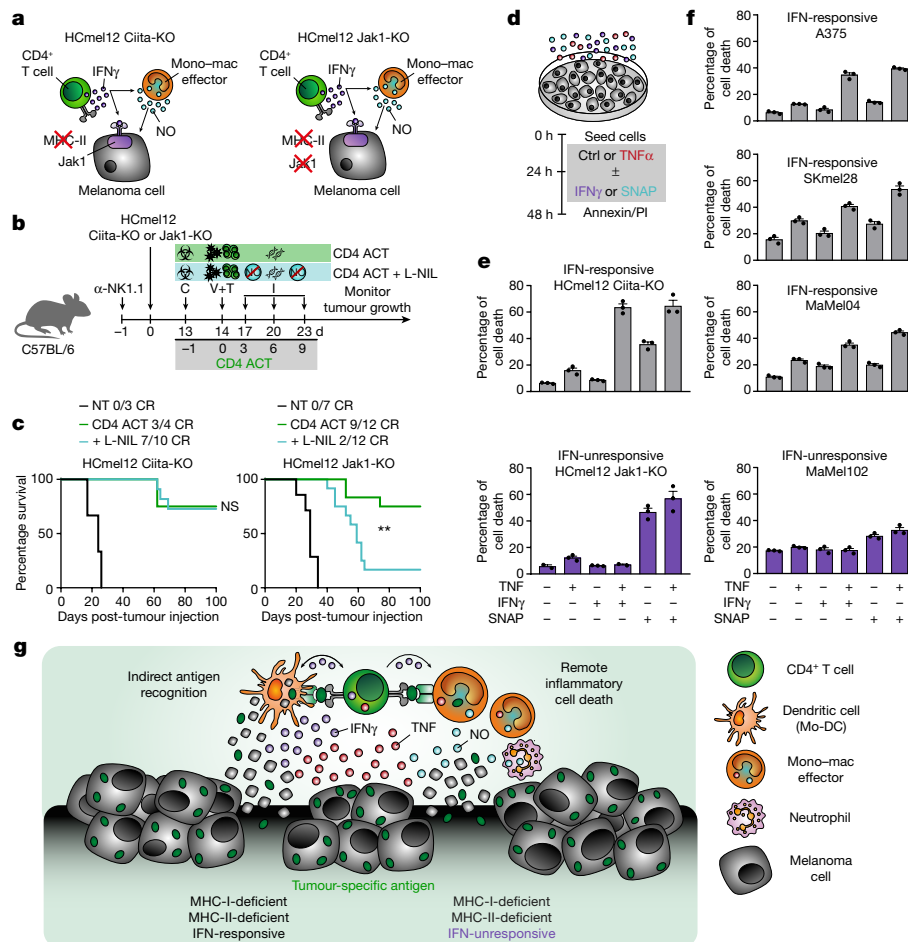


Fig. 4 | CD4⁺ effector T cells cooperate with activated iNOS-expressing tumoricidal monocytes and macrophages to orchestrate remote inflammatory cell death of MHC-deficient and IFN-unresponsive tumours. **a**, Graphical representation of interaction phenotypes of indicated HCmel12 variants. **b**, Experimental treatment protocol to study the impact of chemical iNOS inhibition using L-NIL on CD4 ACT-mediated tumour control. **c**, Kaplan–Meier survival graphs of mice bearing established HCmel12 Ciita-KO melanomas (left) or HCmel12 Jak1-KO melanomas (right) and treated as indicated (NT, non-treated; CR, complete responders; ***P* = 0.0033). Survival was statistically

compared using a log-rank Mantel–Cox test. Means between groups were statistically compared using a one-way ANOVA with Tukey post hoc. **d**, Experimental protocol to assess the ability of the inflammatory mediators TNF, IFN γ and the nitric oxide donor SNAP to induce melanoma cell death. **e, f**, Percentage of cell death in mouse (**e**) and human (**f**) melanoma cells treated as indicated (mean \pm s.e.m. from 2–3 technical replicates). **g**, Graphical summary of inflammatory cell death induction of MHC-deficient and IFN-unresponsive tumours by CD4⁺ T cells in cooperation with iNOS-expressing myeloid cells.

Intravital two-photon microscopy demonstrated that eGFP⁺ TRP-1 CD4⁺ T cells preferentially arrested and engaged in long-lasting close interactions with CD11c-Venus⁺ immune cells only in HCmel12 CRISPR-ctrl tumours, but not in HCmel12 Trp1-KO tumours (Fig. 2h,i, Extended Data Fig. 5g,h and Supplementary Video 5). Antibody-mediated blockade of MHC-II-restricted antigen presentation abrogated the interaction between CD4⁺ T cells and CD11c-Venus⁺ immune cells, confirming the specificity of our findings (Fig. 2j–l and Supplementary Video 6). These observations demonstrate that CD4⁺ effector T cells cluster with CD11c-Venus⁺ immune cells at the tumour invasive margin where they maintain prolonged antigen-specific and MHC-II-restricted interactions that enable them to eradicate MHC-deficient tumours. Of note, CD4⁺ effector T cells also clustered with MHC-II⁺ dendritic antigen-presenting cells and macrophages in human melanomas (Extended Data Fig. 6).

Recruitment of IFN-activated monocytes

Next, we investigated how a comparatively small subpopulation of CD4⁺ effector T cells can eradicate large established tumours. We proposed that adoptively transferred CD4⁺ T cells and injections of synthetic

nucleic acids direct a strong T_H1-associated pathogen defence mechanism that also engages mononuclear phagocytes towards tumour destruction. To explore this hypothesis, we performed scRNA-seq analyses of sorted CD11b⁺ Ly6G⁻ tumour-infiltrating mononuclear phagocytes from mice treated with our CD4 ACT protocol and from non-treated controls. Dimensionality reduction, visualization using uniform manifold approximation and projection (UMAP) and cell type annotation using SingleR showed a clear separation between the monocyte–macrophage clusters derived from CD4 ACT-treated and non-treated tumours (Fig. 3a–c). Differential gene expression and gene set enrichment analyses revealed a strong activation of IFN-response genes on therapy (Fig. 3d and Extended Data Fig. 7a,b).

Unsupervised Leiden clustering of the monocyte–macrophage lineage for CD4 ACT-treated and non-treated groups separated four and seven cell states, respectively. The four cell states in non-treated mice express marker genes characteristic for immature monocytes (NT0), monocyte-derived dendritic cells (NT1), monocyte–macrophage effector cells (NT2) and mature monocytes (NT3). The seven cell states in CD4 ACT-treated mice represent IFN-activated counterparts of the intratumoural monocyte–macrophage network found in non-treated controls (Extended Data Fig. 7c,d). Computation of the

RNA velocity and pseudotime inference revealed a dynamic development of Ly6c-hi inflammatory immature monocytes towards phenotypes of IFN-activated monocyte-derived dendritic cells (ACT1, antigen-presentation phenotype), monocyte–macrophage effectors (ACT2a-c, tumouricidal phenotype) and Ly6c-lo mature monocytes (ACT3a,b, patrolling phenotype) (Fig. 3e and Extended Data Fig. 7e,f).

Flow cytometric analyses of tumour-infiltrating immune cells at days 2, 5 and 8 after adoptive CD4⁺ T cell transfer confirmed the dynamic recruitment of Ly6c-hi immature monocytes into the tumour microenvironment on CD4 ACT therapy and their differentiation into iNOS-expressing tumouricidal mononuclear phagocytes (Fig. 3f and Extended Data Fig. 7g,h). Together, the flow cytometric and transcriptomic analyses indicated that CD4⁺ T cells and innate immune stimuli reprogramme the myeloid network in treated tumours through the recruitment of immature monocytes that acquire IFN-activated cellular states and dynamically differentiate towards MHC-II antigen-presenting and iNOS-expressing tumouricidal effector phenotypes.

Our initial data showed that CD4⁺ effector T cells and innate immune stimulation independently promoted the recruitment of immature monocytes into the tumour microenvironment (Fig. 1j and Extended Data Fig. 2h). Next, we asked whether CD4⁺ T cells and innate immune stimuli synergized on a quantitative or qualitative level for the acquisition of tumouricidal monocyte effector functions. Omitting innate stimuli from our combined ACT therapy regimen reduced the recruitment of neutrophils, but not of immature Ly6c-hi monocytes (Extended Data Fig. 8a,b). However, both CD4⁺ T cells and innate immune stimuli were indispensable for full iNOS induction in the recruited monocytes (Fig. 3g,h and Extended Data Fig. 8b). Functionally, the synergism of the combined therapy was required locally in tumour tissues for the eradication of established tumours, leading to a striking increase in tumour-free survival (Fig. 3i and Extended Data Fig. 8c–e). We proposed that the release of IFN γ was responsible for the CD4⁺ T cell-driven qualitative enhancement of tumouricidal monocyte effector functions on the molecular level. In support of this hypothesis, we found that antibody-mediated neutralization of IFN γ did not influence the absolute number of tumour-infiltrating monocytes and neutrophils, but significantly reduced the frequency of iNOS-expressing monocytes (Fig. 3j,k and Extended Data Fig. 8f,g). IFN γ was essential to eradicate established tumours (Fig. 3l and Extended Data Fig. 8h).

Inflammatory tumour cell death

CD4⁺ T cell-derived IFN γ can either act on tumour cells or through IFN-dependent activation of iNOS-expressing tumouricidal myeloid cells^{18,32–34} (Fig. 4a). Treatment with the highly specific iNOS inhibitor (*N*6-(1-*iminoethyl*)-L-lysine, L-NIL) abrogated the ability of CD4 ACT treatment to control IFN-unresponsive, MHC-deficient HcMel12 Jak1-KO tumours, but had no effect on CD4 ACT treatment of IFN-responsive, MHC-deficient HcMel12 Ciita-KO tumours (Fig. 4b,c and Extended Data Fig. 9a,b). Transient antibody-mediated depletion of CCR2⁺ monocytes impaired the efficacy of CD4 ACT therapy to a greater extent than the depletion of Ly6G⁺ neutrophils, supporting a predominant role of iNOS-expressing monocytes and macrophages for tumour eradication (Extended Data Fig. 9c–e). In aggregate, these results indicated that the ability of adoptively transferred CD4⁺ T cells to indirectly eradicate IFN-unresponsive, MHC-deficient tumour cells involved the remote action of nitric oxide released by IFN-activated tumouricidal myeloid cells.

Our results raised the question as to how myeloid cell-derived nitric oxide contributes to death of IFN-unresponsive tumour cells. Recent data that explained the cytokine driven immunopathology in patients with COVID-19 revealed an inflammatory mode of cell death driven by the concerted action of IFN γ , tumour necrosis factor (TNF) and nitric oxide³⁵. In experiments inspired by these observations, we found that the nitric oxide donor *S*-nitroso-*N*-acetylpenicillamine (SNAP)

effectively induced death of both IFN-responsive HcMel12 Ciita-KO and IFN-unresponsive HcMel12 Jak1-KO melanoma cells in vitro (Fig. 4d,e and Extended Data Fig. 9f,g). IFN γ and TNF were not effective alone and only induced death of IFN-responsive HcMel12 Ciita-KO melanoma cells when used in combination. The ability of the inflammatory mediators to induce cell death was fully recapitulated in a panel of IFN-responsive and IFN-unresponsive human melanoma cell lines (Fig. 4f and Extended Data Fig. 9h). These in vitro results demonstrated that IFN γ sensitizes IFN-responsive melanoma cells towards TNF-induced cell death and suggested that myeloid cell-derived nitric oxide contributes to efficient inflammatory cell death of IFN-unresponsive melanoma cells (Fig. 4g).

Discussion

CD4⁺ T cells have primarily been perceived as helper cells for the activation of CD8⁺ effector T cells³⁶, which kill tumour cells by direct cytotoxicity. In our work, we showed that CD4⁺ effector T cells are also able to independently eradicate established tumours as efficiently as CD8⁺ cytotoxic T cells. Using intravital microscopy, we found that CD4⁺ and CD8⁺ effector T cells differ fundamentally in their mode and their site of action in tumour tissues. Only very few CD4⁺ effector T cells, representing 1% of tumour-infiltrating immune cells, locate at the tumour invasive margins where they interact with CD11c⁺MHC-II⁺ antigen-presenting immune cells and indirectly eliminate tumours. By contrast, much larger numbers of CD8⁺ cytotoxic T cells infiltrate the tumour centre where they directly target and kill MHC-I-expressing tumour cells.

Further innate immune stimulation boosted the T_H1-directed differentiation of CD4⁺ T cells, increased the recruitment of immature monocytes into the tumour microenvironment and supported their IFN-dependent activation and differentiation towards antigen-presenting and iNOS-expressing tumouricidal effector phenotypes. Together, CD4⁺ T cells and IFN-activated mononuclear phagocytes initiate an indirect inflammatory tumour cell death process that acts from the ‘outside-in’ and can be abrogated by neutralizing IFN γ . This unique mode of action operates in parallel to and independent of the direct cytotoxic activities of NK cells³⁷ and enables the eradication of MHC-deficient and IFN-unresponsive tumours that evade direct recognition and destruction by CD8⁺ cytotoxic T cells (Extended Data Fig. 10).

The ability of lymphocytes to cooperate with mononuclear phagocytes for immune defence was first observed in experiments with bacterial infections by investigators trying to understand immune resistance of mice to pathogens and tumours more than 50 years ago^{38,39}. We faithfully recapitulate in our experimental model the cellular and molecular mechanisms underlying this cooperation. MHC-II-dependent antigen presentation by myeloid cells, dynamic IFN-dependent activation and differentiation of the monocyte–macrophage and dendritic cell lineages⁴⁰, and the induction of remote cell death through inflammatory mediators may represent shared immune defence mechanisms that critically contribute to the control of tumours^{33,34,41} and pathogens^{35,42–46}.

Our results have important implications for the future of patient care, as ACT immunotherapies using CD4⁺ T cells have already been successfully implemented in clinical studies. ACT with NY-ESO-1 specific CD4⁺ T cells were used to successfully treat metastatic melanoma⁴⁷ and ACT with CD4⁺ T cells genetically engineered to express an MHC-II–restricted T cell receptor specifically recognizing the cancer germline antigen MAGE-A3 demonstrated clinical efficacy⁴⁸. Our results strongly support the clinical development of ACT-based therapeutic strategies that include appropriate activating stimuli for myeloid cells to unleash the full potential of CD4⁺ T cell effector functions against immune-evasive tumours.


Online content

Any methods, additional references, Nature Portfolio reporting summaries, source data, extended data, supplementary information,

acknowledgements, peer review information; details of author contributions and competing interests; and statements of data and code availability are available at <https://doi.org/10.1038/s41586-023-06199-x>.

1. Tumeah, P. C. et al. PD-1 blockade induces responses by inhibiting adaptive immune resistance. *Nature* **515**, 568–571 (2014).
2. Chen, D. S. & Mellman, I. Elements of cancer immunity and the cancer–immune set point. *Nature* **541**, 321–330 (2017).
3. Waldman, A. D., Fritz, J. M. & Lenardo, M. J. A guide to cancer immunotherapy: from T cell basic science to clinical practice. *Nat. Rev. Immunol.* **20**, 651–668 (2020).
4. Khong, H. T. & Restifo, N. P. Natural selection of tumor variants in the generation of ‘tumor escape’ phenotypes. *Nat. Immunol.* **3**, 7 (2002).
5. McGranahan, N. et al. Allele-specific HLA loss and immune escape in lung cancer evolution. *Cell* **171**, 1259–1271 (2017).
6. Haas, L. et al. Acquired resistance to anti-MAPK targeted therapy confers an immune-evasive tumor microenvironment and cross-resistance to immunotherapy in melanoma. *Nat. Cancer* **2**, 693–708 (2021).
7. Oh, D. Y. et al. Intratumoral CD4⁺ T cells mediate anti-tumor cytotoxicity in human bladder cancer. *Cell* **181**, 1612–1625 (2020).
8. Melenhorst, J. J. et al. Decade-long leukaemia remissions with persistence of CD4⁺ CAR T cells. *Nature* **602**, 503–509 (2022).
9. Veatch, J. R. et al. Neoantigen-specific CD4⁺ T cells in human melanoma have diverse differentiation states and correlate with CD8⁺ T cell, macrophage, and B cell function. *Cancer Cell* **40**, 393–409 (2022).
10. Oliveira, G. et al. Landscape of helper and regulatory antitumor CD4⁺ T cells in melanoma. *Nature* **605**, 532–538 (2022).
11. Rosenberg, S. A. & Restifo, N. P. Adoptive cell transfer as personalized immunotherapy for human cancer. *Science* **348**, 62–68 (2015).
12. Ribas, A. & Wolchok, J. D. Cancer immunotherapy using checkpoint blockade. *Science* **359**, 1350–1355 (2018).
13. Speiser, D. E., Chhijoke, O., Schaeuble, K. & Münz, C. CD4⁺ T cells in cancer. *Nat. Cancer* **4**, 317–329 (2023).
14. Quezada, S. A. et al. Tumor-reactive CD4⁺ T cells develop cytotoxic activity and eradicate large established melanoma after transfer into lymphopenic hosts. *J. Exp. Med.* **207**, 637–650 (2010).
15. Stedzińska, A. et al. Regulatory T cells restrain interleukin-2- and Blimp-1-dependent acquisition of cytotoxic function by CD4⁺ T cells. *Immunity* **52**, 151–166 (2020).
16. Mumberg, D. et al. CD4⁺ T cells eliminate MHC class II-negative cancer cells *in vivo* by indirect effects of IFN- γ . *Proc. Natl Acad. Sci. USA* **96**, 8633–8638 (1999).
17. Corthay, A. et al. Primary antitumor immune response mediated by CD4⁺ T cells. *Immunity* **22**, 371–383 (2005).
18. LaCasse, C. J. et al. Th-1 lymphocytes induce dendritic cell tumor killing activity by an IFN- γ -dependent mechanism. *J. Immunol.* **187**, 6310–6317 (2011).
19. Dhatchinamoorthy, K., Colbert, J. D. & Rock, K. L. Cancer immune evasion through loss of MHC class I antigen presentation. *Front. Immunol.* **12**, 636568 (2021).
20. Pozniak et al. A TCF4/BRD4-dependent regulatory network confers cross-resistance to targeted and immune checkpoint therapy in melanoma. Preprint at *bioRxiv* <https://doi.org/10.1101/2022.08.11.502598> (2022).
21. Overwijk, W. W. et al. Tumor regression and autoimmunity after reversal of a functionally tolerant state of self-reactive CD8⁺ T cells. *J. Exp. Med.* **198**, 569–580 (2003).
22. Muranski, P. et al. Tumor-specific Th17-polarized cells eradicate large established melanoma. *Blood* **112**, 362–373 (2008).
23. Landsberg, J. et al. Melanomas resist T-cell therapy through inflammation-induced reversible dedifferentiation. *Nature* **490**, 412–416 (2012).
24. Kohlmeyer, J. E. Complete regression of advanced primary and metastatic mouse melanomas following combination chemioimmunotherapy. *Cancer Res.* **69**, 6265–6274 (2009).
25. Ribas, A. et al. Overcoming PD-1 blockade resistance with CpG-A Toll-like receptor 9 agonist vidutolimod in patients with metastatic melanoma. *Cancer Discov.* **11**, 2998–3007 (2021).
26. Davar, D. et al. Neoadjuvant vidutolimod and nivolumab in high-risk resectable melanoma. Preprint at *Research Square* <https://doi.org/10.21203/rs.3.rs-2235839/v1> (2022).
27. Foulds, K. E. et al. Cutting edge: CD4 and CD8 T cells are intrinsically different in their proliferative responses. *J. Immunol.* **168**, 1528–1532 (2002).
28. Binnewies, M. et al. Unleashing type-2 dendritic cells to drive protective antitumor CD4⁺ T cell immunity. *Cell* **177**, 556–571.e16 (2019).
29. Ferris, S. T. et al. cDC1 prime and are licensed by CD4⁺ T cells to induce anti-tumour immunity. *Nature* **584**, 624–629 (2020).
30. Cabeza-Cabrerizo, M., Cardoso, A., Minutti, C. M., Pereira da Costa, M. & Reis e Sousa, C. Dendritic cells revisited. *Annu. Rev. Immunol.* **39**, 131–166 (2021).
31. Lindquist, R. L. et al. Visualizing dendritic cell networks *in vivo*. *Nat. Immunol.* **5**, 1243–1250 (2004).
32. Braumüller, H. et al. T-helper-1-cell cytokines drive cancer into senescence. *Nature* **494**, 361–365 (2013).
33. Hung, K. et al. The central role of CD4⁺ T cells in the antitumor immune response. *J. Exp. Med.* **188**, 2357–2368 (1998).
34. Fauskanger, M., Haabeth, O. A. W., Skjeldal, F. M., Bogen, B. & Tveita, A. A. Tumor killing by CD4⁺ T cells is mediated via induction of inducible nitric oxide synthase-dependent macrophage cytotoxicity. *Front. Immunol.* **9**, 1684 (2018).
35. Karki, R. et al. Synergism of TNF- α and IFN- γ triggers inflammatory cell death, tissue damage, and mortality in SARS-CoV-2 infection and cytokine shock syndromes. *Cell* **184**, 149–168 (2021).
36. Borst, J., Ahrends, T., Bąbala, N., Melief, C. J. M. & Kastenmüller, W. CD4⁺ T cell help in cancer immunology and immunotherapy. *Nat. Rev. Immunol.* **18**, 635–647 (2018).
37. Badrinath, S. et al. A vaccine targeting resistant tumours by dual T cell plus NK cell attack. *Nature* **606**, 992–998 (2022).
38. Mackaness, G. B. The immunological basis of acquired cellular resistance. *J. Exp. Med.* **120**, 105–120 (1964).
39. Evans, R. & Alexander, P. Cooperation of immune lymphoid cells with macrophages in tumour immunity. *Nature* **228**, 620–622 (1970).
40. Williams, M., Mildner, A. & Yona, S. Developmental and functional heterogeneity of monocytes. *Immunity* **49**, 595–613 (2018).
41. Hoekstra, M. E. et al. Long-distance modulation of bystander tumor cells by CD8⁺ T cell-secreted IFN γ . *Nat. Cancer* **1**, 291–301 (2020).
42. Locati, M., Curtale, G. & Mantovani, A. Diversity, mechanisms, and significance of macrophage plasticity. *Annu. Rev. Pathol. Mech. Dis.* **15**, 123–147 (2020).
43. Müller, A. J. et al. CD4⁺ T cells rely on a cytokine gradient to control intracellular pathogens beyond sites of antigen presentation. *Immunity* **37**, 147–157 (2012).
44. Olekhovitch, R., Ryffel, B., Müller, A. J. & Bousoo, P. Collective nitric oxide production provides tissue-wide immunity during *Leishmania* infection. *J. Clin. Invest.* **124**, 1711–1722 (2014).
45. Bosteels, C. et al. Inflammatory type 2 cDCs acquire features of cDC1s and macrophages to orchestrate immunity to respiratory virus infection. *Immunity* **52**, 1039–1056.e9 (2020).
46. Simpson, D. S. et al. Interferon- γ primes macrophages for pathogen ligand-induced killing via a caspase-8 and mitochondrial cell death pathway. *Immunity* **55**, 423–441.e9 (2022).
47. Hunder, N. N. et al. Treatment of metastatic melanoma with autologous CD4⁺ T cells against NY-ESO-1. *N. Engl. J. Med.* **358**, 2698–2703 (2008).
48. Lu, Y.-C. et al. Treatment of patients with metastatic cancer using a major histocompatibility complex class II-restricted T-cell receptor targeting the cancer germline antigen MAGE-A3. *J. Clin. Oncol.* **35**, 3322–3329 (2017).

Publisher's note Springer Nature remains neutral with regard to jurisdictional claims in published maps and institutional affiliations.

 **Open Access** This article is licensed under a Creative Commons Attribution 4.0 International License, which permits use, sharing, adaptation, distribution and reproduction in any medium or format, as long as you give appropriate credit to the original author(s) and the source, provide a link to the Creative Commons licence, and indicate if changes were made. The images or other third party material in this article are included in the article's Creative Commons licence, unless indicated otherwise in a credit line to the material. If material is not included in the article's Creative Commons licence and your intended use is not permitted by statutory regulation or exceeds the permitted use, you will need to obtain permission directly from the copyright holder. To view a copy of this licence, visit <http://creativecommons.org/licenses/by/4.0/>.

© The Author(s) 2023

Methods

Patient biopsies

Skin metastases of 20 patients with melanoma (clinical stage III–IV), obtained during routine histopathological diagnostic procedures at the Department of Dermatology of the University Medical Centre Magdeburg, were analysed by immunohistochemistry for the expression of MHC-I (1:100), MHC-II (1:200) and CD8 (undiluted), in addition to the melanoma markers MART-1 (undiluted), gp100 (undiluted), S-100 (undiluted) and Sox10 (undiluted) using the automated Ventana BenchMark platform and standard protocols. These studies were performed in the context of routine clinical workup and were approved by the ethics committee of the Otto-von-Guericke University Hospital Magdeburg (approval number 162/20).

Cell suspensions derived from immunotherapy naive tumour biopsies of 20 melanoma metastases in skin ($n = 5$), subcutis ($n = 4$) and lymph nodes ($n = 11$) from 19 patients (clinical stage IIIB–IV) were analysed for their messenger RNA expression profile in single cells. Methods for tumour dissociation, library construction, scRNA-seq data acquisition and analysis were described previously²⁰. This study was approved by the UZ Leuven Medical Ethical Committee and written consent obtained from all patients. The immune cells were distinguished from other tumour microenvironment cells by high immune signature score and low copy number variation score. Next, the cells were reclustered and annotated using SingleR. The MHC-I and MHC-II gene signature scores were measured using the AUCell R package⁴⁹.

MILAN (mIHC)

Multiplex immunofluorescent images were generated by sequential immunostaining and antibody removal according to the published MILAN protocol⁵⁰ from human melanoma biopsies as described previously⁵⁰. From the complete 41 protein markers included in the published panel, a reduced panel including panCK ($1 \mu\text{g ml}^{-1}$), CD3 ($1 \mu\text{g ml}^{-1}$), CD4 (1:200), CD8, ($1 \mu\text{g ml}^{-1}$), FOXP3 ($1 \mu\text{g ml}^{-1}$), MHC-II ($1 \mu\text{g ml}^{-1}$), CD11c ($1 \mu\text{g ml}^{-1}$), CD68 (1:200), MLANA (1:500), MITF ($1 \mu\text{g ml}^{-1}$) and CD31 ($1 \mu\text{g ml}^{-1}$) for staining keratinocytes, effector T cells, MHC-II expressing myeloid cell subsets, melanoma cells and vessels respectively, is shown. Image analysis was performed as described previously⁵¹. Briefly, stains were visually evaluated for quality by an experienced pathologist. Flat field correction was performed using a custom implementation of the methodology⁵². Consecutive staining rounds were registered using a previously described algorithm⁵³. Tissue autofluorescence was subtracted using a baseline image stained only with a secondary antibody.

Mice

Mice were housed in an ambient temperature- and humidity-controlled environment on a 12-h light/dark cycle to mimic natural conditions. Wild type C57BL/6J mice were purchased from Janvier or Charles River. The T cell receptor-transgenic Pmel-1 (B6.Cg-Thy1a/Cy Tg(Tcr α Tcr β)8Rest/J), TRP-1 (B6.Cg-Rag1tm1Mom Tyrp1B-w Tg (Tcr α ,Tcr β) 9Rest/J), OT-I (C57BL/6-Tg(Tcr α Tcr β)1100Mjb/J) and OT-II (B6.Cg-Tg(Tcr α Tcr β)425Cbn/J) mice, and the fluorescent B6-eGFP (C57BL/6-Tg (UBC-eGFP) 30Scha/J) and CD11c-eYFP (B6.Cg-Tg (Itgax-Venus) 1Mnz) mice were purchased from Jackson Laboratories. Pmel-1-Venus mice were generated by crossing CAG-Venus mice with Pmel-1 mice. TRP-1-eGFP mice were generated by crossing B6-eGFP mice into the TRP-1-deficient Rag1-KO background of TRP-1 mice. OT-I-Venus mice were generated by crossing CAG-Venus mice with OT-I mice. OT-II-dsRed were generated by crossing OT-II mice with hCD2-dsRed mice (kindly provided by C. Halin). All transgenic mice were bred in house. Age matched cohorts of tumour developing mice were randomly allocated to the different experimental groups. All animal experiments were conducted with male mice on

the C57BL/6 background under specific pathogen-free conditions in individually ventilated cages according to the institutional and national guidelines for the care and use of laboratory animals with approval by the Ethics Committee of the Office for Veterinary Affairs of the State of Saxony-Anhalt, Germany (permit licence numbers 42502-2-1393 Uni MD, 42502-2-1586 Uni MD, 42502-2-1615 Uni MD, 42502-2-1672 Uni MD) in accordance with legislation of both the European Union (Council Directive 499 2010/63/EU) and the Federal Republic of Germany (according to §8, section 1 TierSchG and TierSchVersV).

Cell lines and cell culture

The mouse melanoma cell line Hcmel12 was established from a primary melanoma in the Hgf-Cd4k^{R24C} mouse model by serial transplantation in our laboratory as described previously⁵⁴. The mouse melanoma cell line B16 and the human melanoma cell lines A375 and SKmel28 were purchased from ATCC. The human melanoma cell lines MaMel04 and MaMel102 were kindly provided by D. Schadendorf. All cell lines were cultured in complete Roswell Park Memorial Institute (RPMI) medium consisting of RPMI 1640 medium (Life Technologies) supplemented with 10% foetal calf serum (Biochrome), 2 mM L-glutamine, 10 mM non-essential amino acids, 1 mM HEPES (all from Life Technologies), 20 μM 2-mercaptoethanol (Sigma), 100 IU ml⁻¹ penicillin and 100 $\mu\text{g ml}^{-1}$ streptomycin (Invitrogen) in a humidified incubator with 5% CO₂. The cell lines were routinely screened for mycoplasma contamination and were authenticated by the commercial provider or by short tandem repeat fingerprinting.

In vitro cell death assays

For the measurements of cell death in mouse and human melanoma cell lines, cells were first seeded in 96-well plates in complete RPMI medium. Inflammatory mediators were added after 24 h (10 U ml⁻¹ recombinant mouse IFN γ (Peprotech); 1,000 U ml⁻¹ recombinant mouse TNF (Peprotech); 100 U ml⁻¹ animal-free recombinant human IFN γ (Peprotech); 1,000 U ml⁻¹ recombinant human TNF (Peprotech) and 100 μM SNAP (Cayman Chemicals)). After 24 h, floating and adherent cells were gathered and stained using the fluorescein isothiocyanate (FITC) Annexin V Apoptosis Detection Kit I (BD Pharmingen) and analysed using the Attune NxT acoustic focusing flow cytometer (ThermoFisher).

Adenovirus generation and expansion

To generate the adenoviral vaccine Ad-PT, a fusion construct was generated consisting of the first 150 base pairs of the human *PMEL* complementary DNA (coding for amino acids 1–50 of the human *PMEL*/gp100 protein including the CD8⁺ T cell epitope KVPRNQDWL) and 1,404 base pairs of the mouse *Trp1* cDNA (coding for amino acids 51–518 including the CD4⁺ T cell epitope SGHNCGTCRPGWRGAACNQKILTVR) followed by sequences coding for a T2A viral self-cleaving peptide and the yellow fluorescent marker protein eYFP. This vaccine construct was cloned into the pShuttle vector (termed pShuttle-PT-YFP). A recombinant adenovirus vector with this sequence was then generated by a recombinering technique in *Escherichia coli* strain SW102 using bacmid pAdZ5-CV5-E3*. The E1 region of this bacmid is replaced by a selection/counter-selection cassette called ampicillin, LacZ, SacB or the ALS cassette. Next, *E. coli* with this bacmid were electroporated with the PT-YFP transgene with homology arms flanking the ALS cassette obtained by PCR amplification using pShuttle-PT-YFP as a template. Positive colonies were isolated after antibiotic selection on LB-sucrose plates. Ad-PT and Ad-OVA were expanded using the 911 human embryonic retinoblast cell line. A confluent monolayer of the cells in T175 cell culture flasks was infected with Ad-PT or Ad-OVA at MOI 1. The cytopathic effects were observed at around 36 h of incubation at 37 °C. Next, cells were scraped, freeze–thawed three times

Article

and the lysates were cleared by centrifuging at the speed of 7,000g for 45 min. The crude virus was then titrated by the TCID₅₀ method according to standard protocols.

CRISPR–Cas9-mediated genetic cell engineering

To generate Ciita-KO, Trp1-KO, Jak1-KO and Tyr-KO HcMel12 variants, HcMel12 melanoma cells were used that can be readily genetically modified using CRISPR–Cas9-mediated gene editing⁵⁵. Cells were seeded into a 12-well plate at a density of 5×10^5 cells per well and cotransfected with 1.6 µg pX330-sgRNA and 0.4 µg plasmid expressing GFP (pRp-GFP) using Fugene HD transfection reagent (Promega) according to the manufacturer's instructions. GFP positive cells were single-cell sorted using a FACSAria III Cell Sorter (BD) to generate polyclonal and monoclonal populations per targeted gene. HcMel12 cells were mock transfected with pX330 plasmid without single-guide RNA and the polyclonal cell line was used as a CRISPR-control in all performed experiments. Genomic DNA from cultured knockout variants was extracted using the NucleoSpin Tissue kit (Macherey-Nagel) according to the manufacturer's protocol. A two-step PCR protocol was performed to generate targeted PCR amplicons for next-generation sequencing. In the first PCR, specific primers for the target gene with more adapter sequences complementary to the barcoding primers were used to amplify the genomic region of interest with Phusion HD polymerase (New England Biolabs). In a second PCR, adapter-specific universal primers containing barcode sequences and the Illumina adapter sequences P5 and P7 were used (Illumina barcodes D501-508 and D701-D712). Next-generation sequencing was performed with MiSeq Gene and Small Genome Sequencer (Illumina) according to manufacturer's standard protocols with a single-end read and 300 cycles (MiSeq Reagent Kit v.2 300 cycle). For the detection of insertions or deletions, the web-based program Outknocker (<http://www.outknocker.org/>) was used as previously described⁵⁶. FASTQ files were imported, and the sequence of the target gene amplicons was used as reference sequence for alignment.

Western blot

Melanoma cells were lysed using the M-PER mammalian protein reagent (Fermentas) with protease inhibitors (Thermo Scientific). The protein concentration was spectrophotometrically measured by a Bradford-based assay using Pierce BCA protein assay kit (Thermo Scientific) according to manufacturer's protocol. Laemmli buffer was added and lysates were boiled at 95 °C for 5 min. Then, 10 µg of protein was loaded and separated according to size by SDS–PAGE gel electrophoresis on a 3% stacking and 10% polyacrylamide gel. Proteins were transferred to polyvinylidene difluoride membranes with a 0.2 µm pore size (GE Healthcare) by means of wet blotting for 1 h. Unspecific binding was blocked with 5% skimmed milk in PBS with Tween for 1 h. Blots were stained with a goat polyclonal Trp1 antibody (1:1,000, Novus Biologicals) overnight at 4 °C. Next, the blots were incubated with anti-goat IgG HRP (1:2,000, Santa Cruz) for 1 h at room temperature. Horseradish peroxidase conjugated β-actin (200 µg ml⁻¹) was used as loading control. Bound antibody was detected by SignalFire ECL reagent (Cell Signaling Technology) and chemiluminescence was visualized using an OctoPlus QPLEX imager (NH DyeAgnostics).

Retroviral transduction

To generate tagBFP, mCherry and OVA-tagBFP-expressing cell lines, retroviruses were produced by transfecting human embryonic kidney 293T cells with the retroviral packaging constructs pCMV-gag-pol and pMD.2G (expressing VSVg) and the retroviral plasmids pRp-tagBFP, pRp-mCherry and pRp-OVA-tagBFP, respectively, according to standard protocols. Retrovirus-containing supernatant was used to transduce the target cell lines and antibiotic selection of transduced cells was started 48 h after transduction using 10 µg ml⁻¹ Puromycin.

Tumour transplantation experiments

For tumour inoculation, a total of 2×10^5 cells were injected intracutaneously (i.c.) into the shaved flanks or hindlegs of mice with a 30G (0.3 × 13 mm) injection needle (BD). Tumour development was monitored by inspection and palpation. Tumour sizes were measured three times weekly and presented as mean diameter. Mice were euthanized when tumours exceeded 15 mm mean diameter or when mice showed signs of sickness in adherence with the local ethical regulations. All animal experiments were performed in groups of four to six mice and repeated independently at least twice.

ACT therapy protocol

ACT therapy was performed as previously described^{23,24}. In brief, when transplanted melanoma cell lines reached a mean diameter of 3–5 mm, mice were preconditioned for ACT by a single intraperitoneal (i.p.) injection of 2 mg (roughly 100 mg kg⁻¹) of cyclophosphamide in 100 µl of PBS 1 day before intravenous (i.v.) delivery of splenocytes isolated from TCR-transgenic Pmel-1 and/or TRP-1 donor mice harbouring naïve Pmel-1/gp100-specific CD8⁺ T cells and/or naïve TRP-1-specific CD4⁺ T cells (in 100 µl of PBS). Unless otherwise indicated, we transferred splenocytes containing 5×10^5 antigen-specific T cells. The adoptively transferred T cells were stimulated *in vivo* by a single i.p. injection of 2.5×10^8 PFU of the recombinant adenoviral vaccine Ad-PT in 100 µl of PBS. On day 3, 6 and 9 after T cell transfer, tumours were injected with 50 µg of CpG 1826 (MWG Biotech) and 50 µg of polyinosinic:polycytidylic acid (polyI:C, Invivogen) diluted in 100 µl of distilled water. Seven days after T cell transfer, blood was taken routinely from the *Vena facialis* to confirm successful expansion of transferred T cells by flow cytometry.

Supplementary *in vivo* treatments

NK-cell depletion was performed by a single i.p. injection of 200 µg anti-NK1.1 antibody (clone PK136, BioXCell) in 100 µl, diluted in pH 7.0 Dilution Buffer (BioXCell). CD8⁺ T cell depletion was performed by i.p. injections of initially 100 µg, followed by weekly injections of 50 µg of anti-CD8 antibody (clone 2.43, BioXCell). MHC-II blockade was performed by a single i.v. injection of 500 µg of anti-MHC-II antibody (clone Y-3P, BioXCell) directly after inducing anaesthesia for 2P-IVM and roughly 30 to 60 min before data acquisition. IFNγ blockade was performed by weekly i.p. injection of 500 µg of anti-IFNγ antibody (clone XMGL2, BioXCell) in 100 µl, diluted in pH 8.0 buffer. Monocyte depletion was performed by i.p. injections of 20 µg of anti-CCR2 (clone MC21, provided by M. Mack) for five consecutive days. Neutrophil depletion was performed by i.p. injections of 100 µg of anti-Ly6G (clone 1A8, BioXCell) every fifth day. Inhibition of iNOS was performed by daily i.p. injection of 200 µg of L-NIL (Cayman Chemicals) diluted in 100 µl of PBS.

Flow cytometry

Immunostaining of single-cell suspensions was performed according to standard protocols. Single suspensions were incubated with anti-CD16/CD32 (1:300, Biolegend) before staining with fluorochrome-conjugated monoclonal antibodies CD45-APC Fire 750 (1:1,600), CD11c-APC (1:200), F4/80-PE (1:300), CD11b-BV711 (1:200), Ly6C-PE-Cy7 (1:2,000), CD45R-PE (1:1,000), CD3ε-BV421 (1:500), CD4-BV605 (1:500), NK1.1-APC (1:400), CD45-FITC (1:1,000), F4/80-APC (1:200), Ly6C-BV421 (1:800), iNOS-PE, (1:300), I-A/I-E-BV510 (1:800), CD45-BV711 (1:200), CD11c-APC Fire 750 (1:100), Siglec H-FITC (1:400), CD4-PE (1:1,600), CD11b-PE-Cy7 (1:2,000), Ly6G-PE (1:800), CD3ε-BV711 (1:100), CD8α-APC Fire 750 (1:1,600), H2-Kb-PE (1:500), I-A/I-E-APC (1:2,000), CD3ε-FITC (1:100), CD335-APC (1:100), CD8α-PE (1:800), Vβ14-FITC (1:2,000), T-bet-PeCy7 (1:200) and Foxp3-Alexa Fluor 647 (1:100). Intracellular staining was carried out using a Fixation/Permeabilization Solution Kit (BD or Biolegend). Single-cell suspensions from tumours were

first stained with antibodies against cell-surface antigens, then fixed and permeabilized, followed by intracellular staining. Dead cell exclusion was performed using 7-aminoactinomycin or propidium iodide. All data were acquired with an Attune NxT acoustic focusing flow cytometer (ThermoFisher). Gating and subsequent analyses were performed using FlowJo v.10.8.1 for Windows (Tree Star, Inc.). Fluorescence-activated cell sorting was performed using an Aria III (BD Biosciences).

Quantification of tumour-infiltrating immune cells

To quantify the abundance of immune cell subpopulations in tumour tissues, 2,000 cells of interest per biological sample were concatenated to a single FCS file. The *t*-distributed stochastic neighbor embedding (*t*-SNE) plots were generated in FlowJo using the opt-SNE learning configuration⁵⁷. The vantage-point tree *K*-nearest-neighbours algorithm and the Barnes–Hut gradient algorithm were set to 1,000 iterations, 30 perplexity and 840 learning rate. Immune cell subpopulations were annotated on the basis of heatmaps for characteristic marker combinations and their percentage in the tumour was calculated.

Analysis of tumour cell MHC expression and antigen recognition by CD4⁺ T cells

To quantify the expression of MHC molecules, tumour cells were pretreated with 100 U ml⁻¹ recombinant murine IFN γ (Peprotech) for 72 h and then analysed by flow cytometry. To assess antigen recognition by CD4⁺ T cells, TRP-1 TCRtg mice were immunized with Ad-PT and subsequently injected with 50 μ g of CpG and 50 μ g of poly:I.c.i.c. 3 and 6 days after immunization. TRP-1 CD4⁺ T cells were isolated from the spleen and purified by two rounds of magnetic cell sorting (Miltenyi). Direct antigen recognition was determined by coculturing purified CD4⁺ T cells with IFN γ pretreated Hcme12 cells. Antigen recognition in proxy was assessed by initially generating bone marrow-derived dendritic cells with recombinant GM-CSF and IL-4 (Peprotech) as previously described. After 1 week, differentiated bone marrow-derived dendritic cells were then pulsed overnight with Hcme12 lysate, before coculture with purified CD4⁺ T cells. For both direct and myeloid cell-dependent antigen-recognition assays, the production of IFN γ from the CD4⁺ T cells was measured 16 h after coculture by intracellular cytokine staining using flow cytometry according to standard protocols.

Calculations of absolute immune cell counts in tumour tissues

Tumours were excised with tweezers and scissors, then weighed using the Entris 224-1S analytical balance (Sartorius). Single-cell suspensions were created mechanically using 5-ml syringe plungers (BD) and 70 μ m cell strainers (Greiner). After immunostaining, cells were suspended in a defined volume and analysed on the Attune NxT acoustic focusing flow cytometer that uses a unique volumetric sample and sheath fluid delivery system allowing for accurate measurements of the number of cells analysed in a defined sample volume. The total number of viable CD45⁺ immune cells in an individual tumour can then be derived by multiplying the number of CD45⁺ immune cells counted in a defined sample volume with the total volume of the respective single-cell suspension. Division of this total number by the total weight of the tumour yields the absolute immune cell count per mg tumour tissue. The absolute count of various immune cell subpopulations was calculated from their relative percentage in viable CD45⁺ immune cells.

Immunofluorescence microscopy

Tumours were harvested on day 5 after ACT and fixed in 4% paraformaldehyde for 24 h, then dehydrated in 20% sucrose before embedding in optimal cutting temperature freezing media (Sakura Finetek). Next, 6 μ m sections were cut on a CM305S cryostat (Leica), adhered

to Superfrost Plus slides (VWR) and stored at -20°C until further use. When thawed, slides were either fixed with ice-cold acetone and stained with rat anti-mouse I-A/I-E (1:50) and anti-rat IgG-Alexa Fluor 594 (1:100) or directly mounted with Vectashield Antifade Mounting Medium (Vector Laboratories). Images were acquired on an Axio Imager.M2 with a Colibri 7 LED illumination system (Zeiss) and analysed with ImageJ v.1.52i (<http://imagej.nih.gov/ij>).

Intravital two-photon microscopy

Mice were anaesthetized with 100 mg kg⁻¹ ketamine and 10 mg kg⁻¹ xylazine i.p., complemented by 3 mg kg⁻¹ acepromazine s.c. after the onset of anaesthesia. The animals were placed and fixed to a heated stage. Transparent Vidisc carbomer gel was applied to moisten the eyes during anaesthesia. The hind leg was fixed in an elevated position and the skin covering the melanoma was detached using surgical scissors and forceps. One drop of transparent Vidisc carbomer gel was used on the exposed site as mounting medium. Two component STD putty (3M ESPE) placed on both sides of the leg was used to create a level surface using a 24 \times 60 mm cover slip, which was gently pressed on the putty in a way that the coverslip made slight contact with the exposed site, without exerting pressure on the tumour. After complete polymerization of the putty, the mice were transferred onto a 37 $^{\circ}\text{C}$ heating plate under the two-photon microscope.

Imaging was performed using distilled water or transparent Vidisc carbomer gel as immersion liquid with a W Plan-Apochromat $\times 20/1.0$ DIC VIS-IR objective mounted to a Zeiss LSM 700 upright microscope with the ZEN software environment (v.2.1, Zeiss), or a LaVision TrimScope mounted to an Olympus BX50WI fluorescence microscope stand and a XLUMPlanFl $\times 20/0.95$ objective. Excitation on the LSM700 setup was performed with Mai Tai DeepSee (tuned to 800 nm) and Insight X3 (tuned to 980 nm) Ti:Sa oscillators (both from Spectra-Physics). Fluorescence signals were read out on a long-pass dichroic mirror detector cascade as follows: dsRed, 980 nm excitation and 555 nm dichroic transmission with a 587/45 nm bandpass filter; Venus, 980 nm excitation and 520 nm dichroic transmission with a 534/30 nm bandpass filter; second-harmonic generation, 800 nm excitation and 445 nm dichroic deflection unfiltered; tagBFP, 800 nm excitation and 490 nm dichroic deflection with a 485 nm short-pass filter; and eGFP, 980 nm excitation, 520 nm dichroic deflection and 490 nm dichroic transmission with a 525/50 nm bandpass filter. Excitation on the TrimScope setup was performed with a Chamaeleon Ultra II Ti:Sa oscillator tuned to 880 nm. Fluorescence signals were read out with a double split detector array with a 495 nm main dichroic mirror and 445 and 520 nm secondary dichroic mirrors (all long-pass) as follows: second-harmonic generation, 495 nm and 445 nm dichroic deflection unfiltered; tagBFP, 495 nm dichroic deflection and 445 nm dichroic transmission with a 494/20 nm bandpass filter; eGFP, 495 nm dichroic transmission and 520 nm dichroic deflection with a 514/30 nm bandpass filter; and Venus, 495 nm and 520 nm dichroic transmission with a 542/27 nm bandpass filter. Non-descanned photomultiplier tubes (for second-harmonic generation, dsRed and Venus in all setups, and for eGFP and tagBFP in the TrimScope setup) and high sensitivity detectors (for tagBFP and eGFP in the Zeiss setup) were used for signal collection.

Typically, three to four representative fields of view of 353 μm^2 size in *x*-, *y*- and *z*-range of 48 to 60 μm with 4 μm step sizes were chosen for data acquisition. *Z*-stacks were captured in 60–90 s intervals and individual video length was 15–30 min. Data analysis was performed with the Bitplane Imaris software (v.8.3 to 9.7). T cells were identified using the Imaris spot function. Tumour area was identified using the surface function with low surface detail. CD11c-Venus cells were identified using the surface function with high detail. T cell speed was calculated using the Imaris software. Cells were considered arrested when speed was less than 2 $\mu\text{m min}^{-1}$. Contact duration was measured as the time that the distance between the centre of mass of a T cell to the closest CD11c cell surface was less than 8 μm . Snapshot images of 3D rendering and

tracking were cropped, arranged and animated for time series using ImageJ v.1.52i (<http://imagej.nih.gov/ij>).

Cell preparation for scRNA-seq

Three individual tumours per group were harvested and processed into single suspensions. CD45⁺ cells were enriched using a positive selection kit (Miltenyi). Next, individual samples were hashtagged with unique TotalSeq-B hashtag antibodies B0301-B0310 (1:300, Biolegend) and subsequently stained with fluorescently labelled antibodies. CD45⁺CD11b⁺Ly6G⁻ cells were sorted with an Aria III fluorescence-activated cell sorter (BD). Isolated cells were loaded onto one lane of a 10X Chromium microfluidics controller. cDNA of hashtag and gene expression libraries were amplified, and indices added by means of PCR. Sequencing was performed on an Illumina Novaseq on two lanes of a S1 cartridge with 150 bp read length in paired end mode. Reading depth was calculated to obtain roughly 50,000 reads per cell for the gene expression library and 5,000 reads per cell for the hashtag library.

scRNA-seq data processing and hashtag-demultiplexing

The scRNA-seq data generated using 10X Genomics Chromium technology were aligned and quantified using the Cell Ranger Single-Cell Software Suite against the mm10 mouse reference genome. The raw, unfiltered data generated from Cell Ranger were used for downstream analyses. Quality control was performed on cells on the basis of the three metrics: total unique molecular identifier (UMI) count, number of detected genes and proportion of mitochondrial gene count per cell. Specifically, cells with less than 1,000 UMIs, 1,000 detected genes and more than 25% mitochondrial UMIs were filtered out. To remove potential doublets, cells with UMI count above 40,000 were removed. Subsequently, we demultiplexed the samples tagged with distinct hashtag-oligonucleotides using Solo⁵⁸. After quality control, we normalized raw counts by their size factors using scran⁵⁹ and subsequently performed log₂ transformation. The logarithmized and normalized count matrix was used for the downstream analyses.

Dimensionality reduction, unsupervised clustering and differential gene expression analyses

Analysis of normalized data was performed using the scanpy Python package⁶⁰. Initially, the 4,000 most highly variable genes were selected for subsequent analysis using `scanpy.pp.highly_variable_genes` with the parameter `'n_top_genes=4000'`. Next, a principal component analysis was performed with 50 components using `scanpy.tl.pca` with the parameters `'n_comps=50, use_highly_variable=True, svd_solver="arpack"`. Subsequently, dimensionality reduction was performed using UMAP with `scanpy.tl.umap`. Single cells were automatically assigned using R package SingleR⁶¹, with transcriptomes from the Immunological Genome Project as a reference. Clustering of single cells by their expression profiles was conducted by using the Leiden algorithm running `scanpy.tl.leiden` with the parameter `'resolution=1.0'`. Clusters with fewer than 20 cells were removed from further analysis. Differential gene expression was performed between cells classified as macrophages and monocytes from non-treated and CD4 ACT-treated mice using a hurdle model implemented in the R package MAST. Subsequent gene set enrichment analysis was performed using gene set enrichment analysis in preranked mode using the log₂ fold change as a ranking metric. The IFN score was derived by calculating a z-score for all genes from the MSigDB gene set 'HALLMARK_INTERFERON_GAMMA_RESPONSE' for each cell.

RNA velocity

For RNA velocity, count matrices of spliced and unspliced RNA abundances were generated using the velocity workflow for 10X chromium samples, with the genome annotation file supplied by 10X Genomics

for the mm10 genome and a repeat annotation file retrieved from the UCSC genome browser. Subsequent analyses were performed using scVelo⁶². The count matrices were loaded into the scanpy environment, merged with the previously generated anndata objects and normalized using `scvelo.pp.filter_and_normalize`. Next, moments for velocity estimation were calculated, gene-specific velocities were estimated and the velocity graphs were computed. Furthermore, a partition-based graph abstraction was generated with velocity-directed edges.

Statistical methods

Statistical analyses and number of samples (*n*) are given in each figure legend. Mann–Whitney *U*-tests, unpaired two tail *t*-tests, analysis of variance (ANOVA) and log-rank tests were performed in Graphpad Prism (v.8).

Reporting summary

Further information on research design is available in the Nature Portfolio Reporting Summary linked to this article.

Data availability

The raw sequencing mouse scRNA-seq data are available at the NCBI GEO under the accession GSE230427 without restrictions. The normalized and logarithmized count matrix used for the subsequent analyses is also available at the NCBI GEO under the accession GSE230427 without restrictions. Human scRNA-seq data used in this study are available at the European Genome-Phenome Archive with the identifier EGAS00001006488, available for non-commercial research purposes on reasonable request and subject to review of a project proposal that will be evaluated by the VIB-UZL Data Access Committee. Source data are provided with this paper.

49. Aibar, et al. SCENIC: single-cell regulatory network inference and clustering. *Nat. Meth.* **14**, 1083–1086 (2017).
50. Bolognesi, M. M. et al. Multiplex staining by sequential immunostaining and antibody removal on routine tissue sections. *J. Histochem. Cytochem.* **65**, 431–444 (2017).
51. Antoranz, A. et al. Mapping the immune landscape in metastatic melanoma reveals localized cell–cell interactions that predict immunotherapy response. *Cancer Res.* **82**, 3275–3290 (2022).
52. Kask, P., Palo, K., Hinnah, C. & Pommerencke, T. Flat field correction for high-throughput imaging of fluorescent samples. *J. Microsc.* **263**, 328–340 (2016).
53. Reddy, B. S. & Chatterji, B. N. An FFT-based technique for translation, rotation, and scale-invariant image registration. *IEEE Trans. Image Process.* **5**, 1266–1271 (1996).
54. Bald, T. et al. Ultraviolet-radiation-induced inflammation promotes angiotropism and metastasis in melanoma. *Nature* **507**, 109–113 (2014).
55. Mengoni, M., Braun, A. D., Gaffal, E. & Tüting, T. The aryl hydrocarbon receptor promotes inflammation-induced dedifferentiation and systemic metastatic spread of melanoma cells. *Int. J. Cancer* **147**, 2902–2913 (2020).
56. Schmid-Burgk, J. L. et al. OutKnocker: a web tool for rapid and simple genotyping of designer nuclease edited cell lines. *Genome Res.* **24**, 1719–1723 (2014).
57. Belkina, A. C. et al. Automated optimized parameters for t-distributed stochastic neighbor embedding improve visualization and analysis of large datasets. *Nat. Commun.* **10**, 5415 (2019).
58. Bernstein, N. J. et al. Solo: doublet identification in single-cell RNA-seq via semi-supervised deep learning. *Cell Syst.* **11**, 95–101.e5 (2020).
59. Lun, A. T. L., McCarthy, D. J. & Marioni, J. C. A step-by-step workflow for low-level analysis of single-cell RNA-seq data with Bioconductor. *F1000 Res.* **5**, 2122 (2016).
60. Wolf, F. A., Angerer, P. & Theis, F. J. SCANPY: large-scale single-cell gene expression data analysis. *Genome Biol.* **19**, 15 (2018).
61. Aran, D. et al. Reference-based analysis of lung single-cell sequencing reveals a transitional profibrotic macrophage. *Nat. Immunol.* **20**, 163–172 (2019).
62. Bergen, V., Lange, M., Peidli, S., Wolf, F. A. & Theis, F. J. Generalizing RNA velocity to transient cell states through dynamical modeling. *Nat. Biotechnol.* **38**, 1408–1414 (2020).

Acknowledgements We thank the following individuals for their support: S. Bonifatius, J. Herz, J. Leibold, A. Ziemis, K. Beinhoff, R. Hartig and J. Dudeck for managing the mouse colony, performing tumour analyses and assisting for intravital microscopy and cell sorting; M. Mack for providing us with the anti-CCR2 mAb; J. Ruotsalainen for supporting viral vector production and CRISPR-Cas9 gene editing and D. Schanze for sequencing of CRISPR-Cas9 engineered cells. T.T. was supported by funding from the German Research Foundation (grant nos. SFB854-P27 and SFB704-P22, FOR5489-P8, TU 90/10-1) and the German Cancer Aid (grant nos. 70112525 and 70114549). A.J.M. was supported by funding from the European Research

Council under the European Union's Horizon 2020 research and innovation programme (StG ImmProDynamics, grant agreement no. 714233) and the German Research Foundation DFG (grant nos. SFB854-Z01, SFB854-B31). W.K. was supported by funding from the German Research Foundation DFG (grant no. CRC TRR 338). J.C.M. received funding within the Grand Challenges Program of VIB, from FWO/KOTK (grant no. GOB1622N), Neftkens foundation, KULeuven (C1 grant) and the Belgian Excellence of Science programme. A.C.B. and M.M. were funded by the Else Kröner-Fresenius Forschungskolleg Magdeburg (grant nos. 2017_Kolleg.07; TP3 and TP4).

Author contributions B.K., A.C.B., N.S., S.G., K.K., P.D., S.H., T.C.v.D.S., Y.F. and A.K. performed experiments and analysed data. B.K., N.S. and J. Peters generated cell lines. N.S., D.Y. and M.E. generated recombinant adenoviruses. M.M., A.D.B. and O.B. collected clinical data. A.D.B., J. Pozniak, F.R., J.-C.M. and R.G. performed scRNA-seq analyses. B.K., A.C.B., N.S., A.A., S.G., A.J.M. and T.T. designed experiments. A.A. and F.M.B. generated the MILAN images. B.K. and A.J.M. performed and analysed the intravital images and videos. B.K., A.C.B., N.S., A.D.B., E.G.,

S.K., D.M., H.K., J.-C.M., W.K., A.J.M. and T.T. contributed intellectual input and helped to interpret data. A.J.M. and T.T. led the research programme. B.K., A.C.B., A.D.B., W.K., A.J.M. and T.T. wrote the manuscript.

Competing interests The authors declare no competing interests.

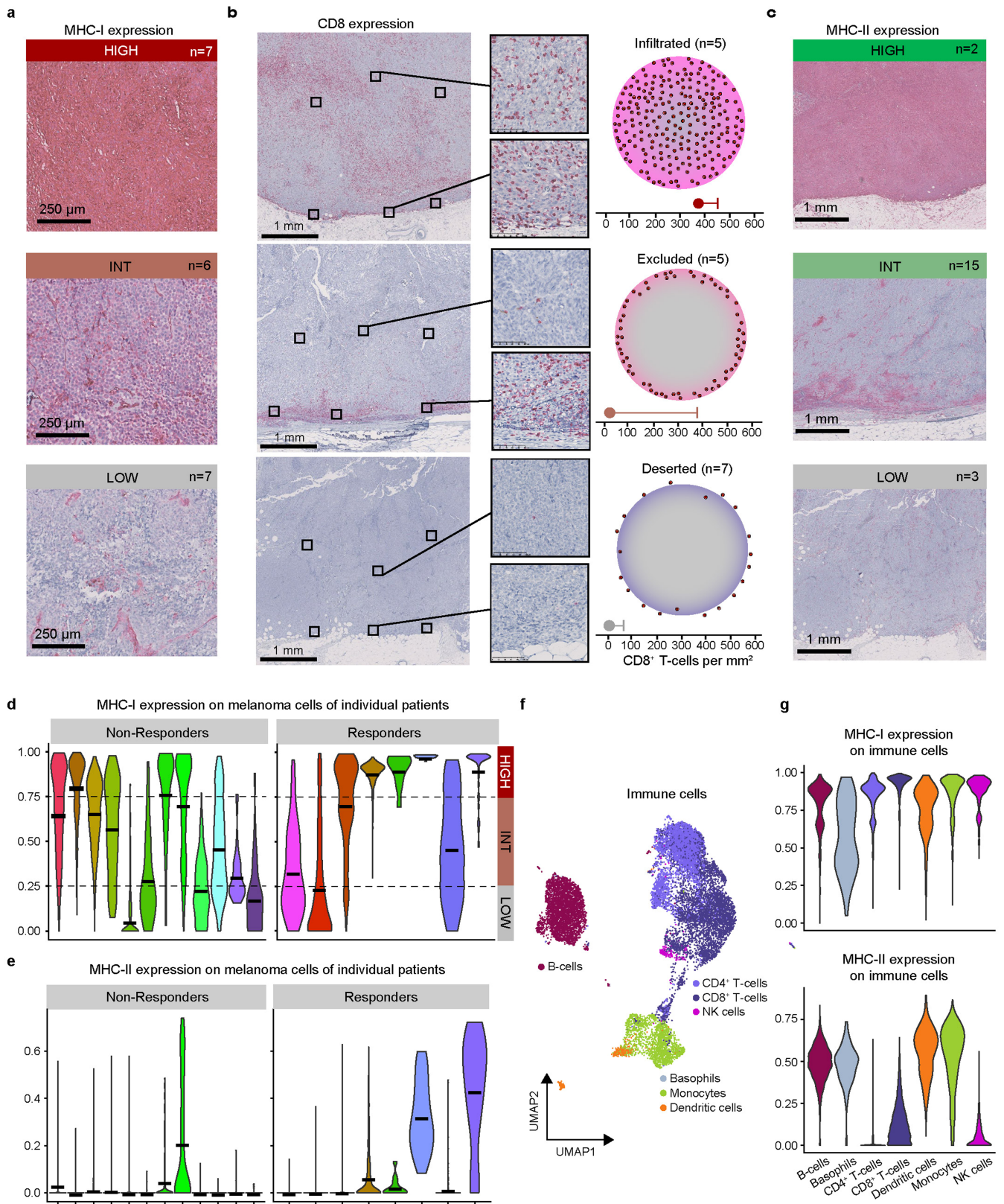
Additional information

Supplementary information The online version contains supplementary material available at <https://doi.org/10.1038/s41586-023-06199-x>.

Correspondence and requests for materials should be addressed to Andreas J. Müller or Thomas Tüting.

Peer review information *Nature* thanks Carl Figdor, Aude Chapuis and the other, anonymous, reviewer(s) for their contribution to the peer review of this work. Peer reviewer reports are available.

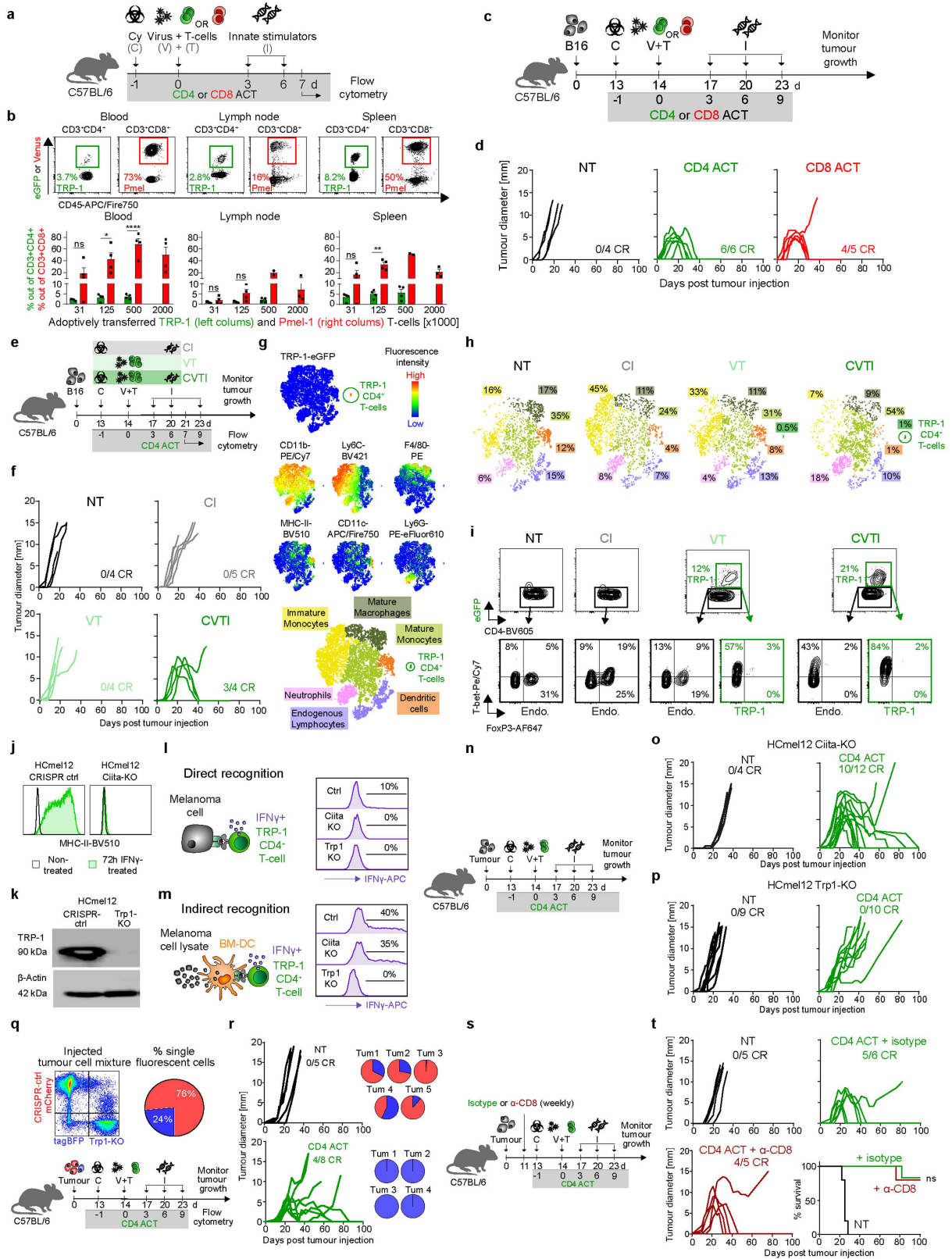
Reprints and permissions information is available at <http://www.nature.com/reprints>.



Extended Data Fig. 1 | See next page for caption.

Extended Data Fig. 1 | Landscapes of MHC expression, distribution of tumour infiltrating CD8+ T cells, and single cell transcriptomes of human melanoma metastases. a, Representative immunohistochemical stains of human melanoma skin metastases with high, intermediate and low expression of MHC-I. b, Left: Overviews of representative immunohistochemistry stainings for CD8 and magnifications of 0.1 mm² squares in the tumour center and at the tumour invasive margins that were evaluated for the number of infiltrating CD8+ T cells; Right: graphical illustration of the three distinct patterns of immune infiltration observed. c, Representative immunohistochemical stains of human melanoma skin metastases with high, intermediate and low expression

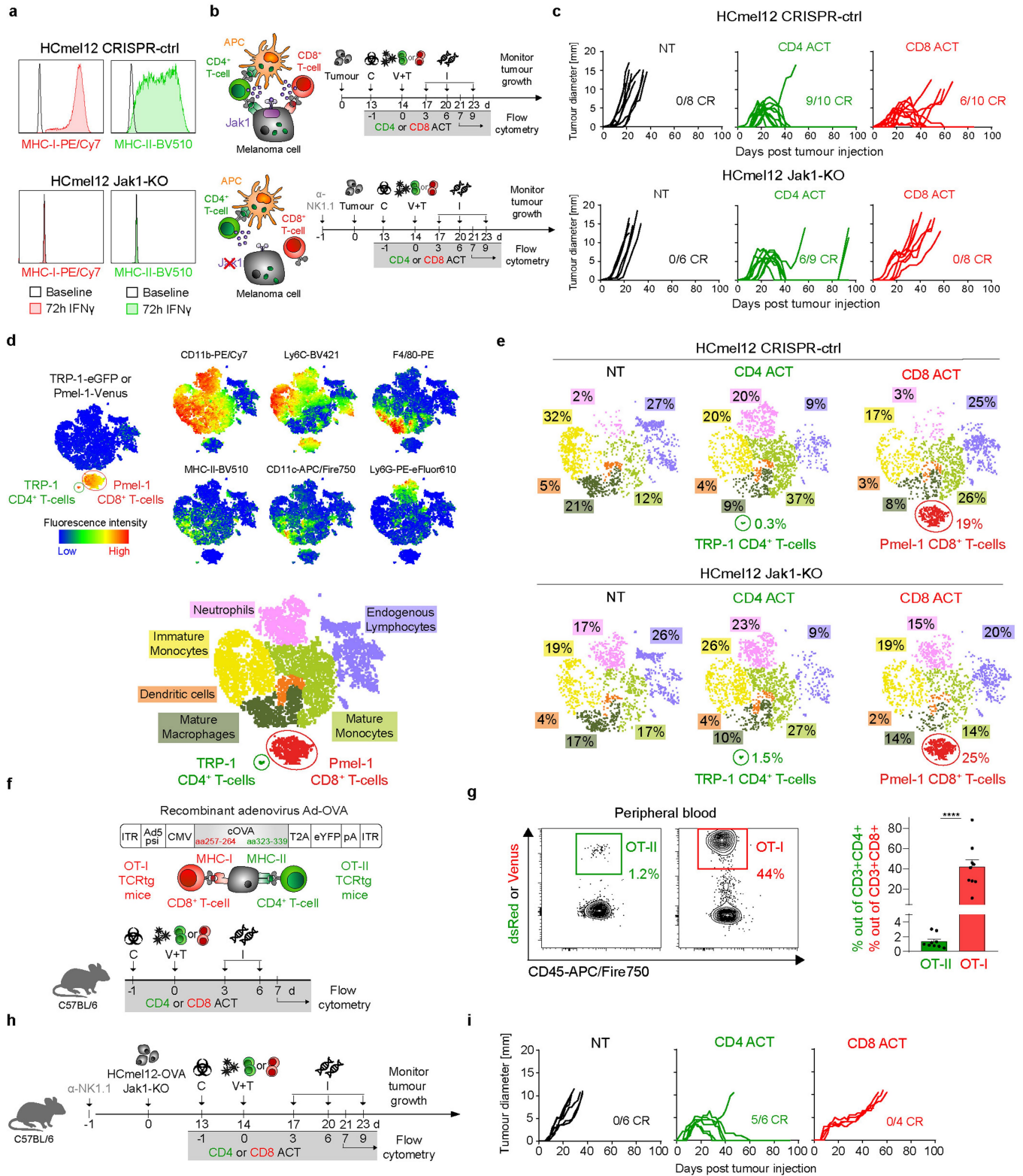
of MHC-II. d, MHC-I and (e) MHC-II gene set expression in single melanoma cells of an additional set of human melanoma metastases in skin (n = 5), subcutis (n = 4), and lymph nodes (n = 11), categorised into ICB therapy responders and non-responders. Median MHC-I gene set expression was used to categorize tumours according to high (>0.75), intermediate (0.25 · 0.75) and low (<0.25) expression levels. f, Uniform manifold approximation and projection (UMAP) clustering of the immune cell compartment in human melanomas annotated as indicated. g, MHC-I (top) and MHC-II (bottom) gene set expression in the indicated immune cell subpopulations.



Extended Data Fig. 2 | See next page for caption.

Extended Data Fig. 2 | Establishment of an experimentally tractable adoptive cell transfer model to compare CD4+ and CD8+ T-cell effector functions against tumours and eradication of established MHC-II-deficient melanomas through indirect antigen recognition on MHC-II+ tumour-infiltrating immune cells. a, Experimental protocol to assess the *in vivo* expansion of adoptively transferred CD8+ and CD4+ T cells. b, Representative flow cytometric contour plots with 0.5×10^6 transferred cells (top) and quantitation of Pmel-1 CD8+ and TRP-1 CD4+ TCRtg T-cell expansion in peripheral blood, lymph nodes and spleen 7 days after ACT (bottom, mean \pm SEM from $n = 2-4$ biologically independent samples; **** $p < 0.0001$, ** $p = 0.0010$, * $p = 0.0146$ by one-way ANOVA with Tukey's post-hoc test). c, e, Experimental protocols for adoptive cell transfer (ACT) immunotherapy of established tumours in mice and flow cytometric analyses of tumour-infiltrating immune cells. d, f, Individual tumour growth curves of established B16 melanomas treated as indicated. g, t-SNE heatmaps of multiparametric flow cytometry for B16 melanoma single cell suspensions showing the indicated markers (top) and corresponding annotation (bottom) of TRP-1 CD4+ T-cells (GFP⁺), immature monocytes (CD11b⁺ Ly6C^{hi}), mature monocytes (CD11b⁺ Ly6C^{lo}), mature macrophages (CD11b⁺ F4/80⁺), dendritic cells (CD11b⁺ MHC-II⁺ CD11c⁻), endogenous lymphocytes (CD11b⁻ CD11c⁺), and neutrophils (CD11b⁺ Ly6G⁺). h, Annotated t-SNE plots quantifying the immune cell composition of B16 melanomas treated as indicated. i, Representative flow cytometric contour plots for the phenotyping of endogenous and transferred (VT, CVT1, green)

CD4+ T-cells from mice treated as indicated. j, Representative flow cytometric histograms for MHC-II expression on indicated melanoma cells cultivated in the presence or absence of IFN γ . k, Representative western blot analysis for TRP-1 expression for the indicated melanoma cells ($n = 2$ biologically independent samples). Beta-actin was used as a loading control. For uncropped images see source data table. l, Graphical representation of direct and (m) indirect recognition of melanoma cells by CD4+ T-cells (left) and representative flow cytometry histograms showing IFN γ ⁺ TRP-1 CD4+ T-cells following stimulation by the indicated melanoma cells (right). n, Experimental protocol and (o, p) individual tumour growth curves of established B16 melanomas treated as indicated. q, Injection of a tumour cell mixture consisting of -75% Hcmel12 CRISPR-ctrl cells and -25% Hcmel12 Trp1-KO cells (top) and treatment protocol (bottom). r, Individual tumour growth curves of mice bearing established melanomas and treated as indicated (left) and proportion of Hcmel12 CRISPR-ctrl and Hcmel12 Trp1-KO cells from escaping tumours (right). s, Experimental treatment protocol for depletion of CD8+ T-cells during CD4 ACT. t, Individual tumour growth curves and Kaplan-Meier survival graph of mice bearing established Hcmel12 CRISPR-ctrl melanomas treated as indicated. Means between groups were statistically compared using one-way ANOVA with Tukey's post-hoc test. Survival was statistically compared using a log-rank Mantel-Cox test. NT, non-treated; C, cyclophosphamide; V, Ad-PT; T, TCRtg TRP-1 CD4+ T-cells; I, innate stimuli, polyI:C and CpG; CR, complete responders.

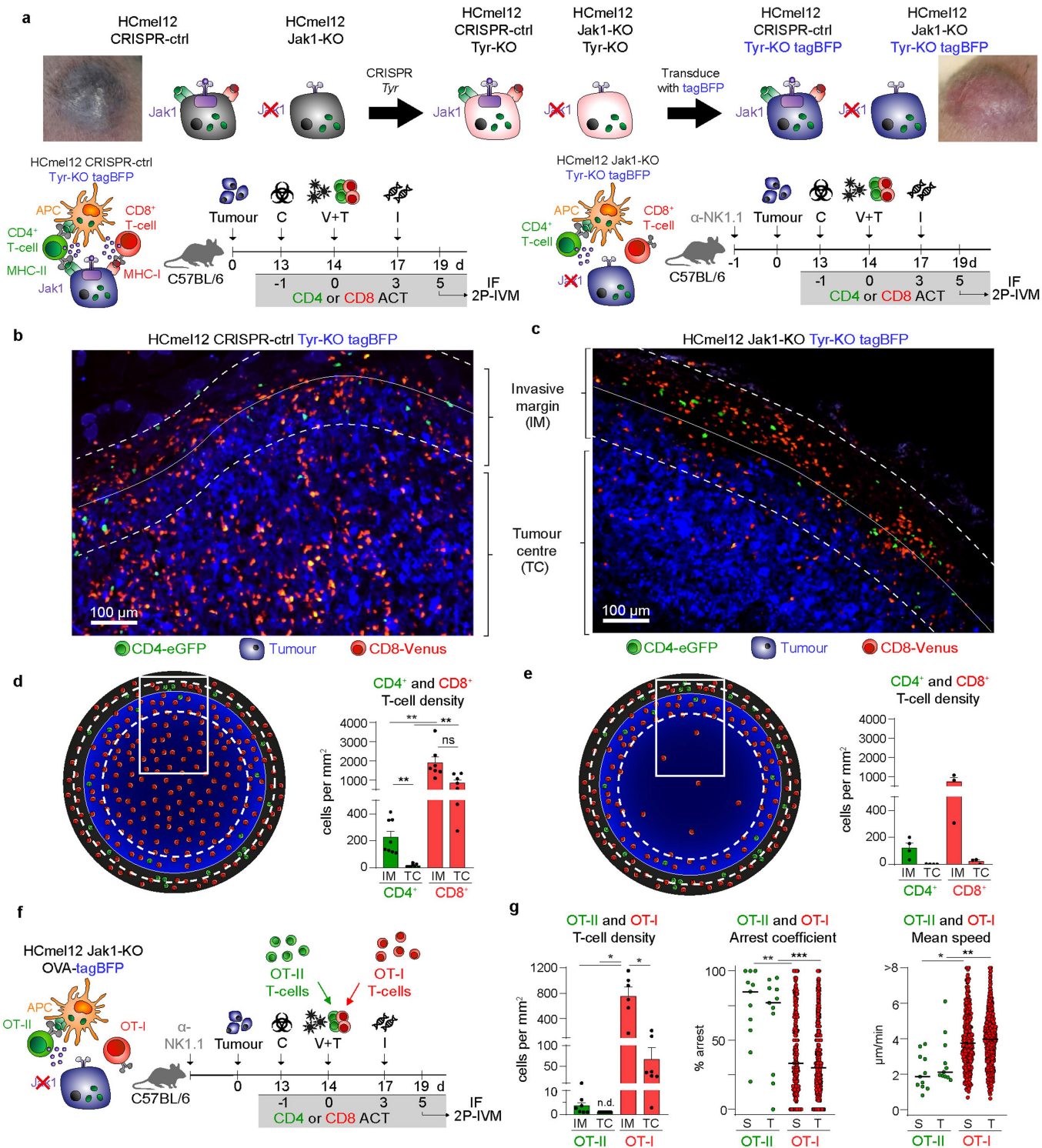


Extended Data Fig. 3 | See next page for caption.

Extended Data Fig. 3 | Comparative evaluation of CD4+ and CD8+ T-cell effector functions against IFN-unresponsive tumours lacking MHC-I and MHC-II.

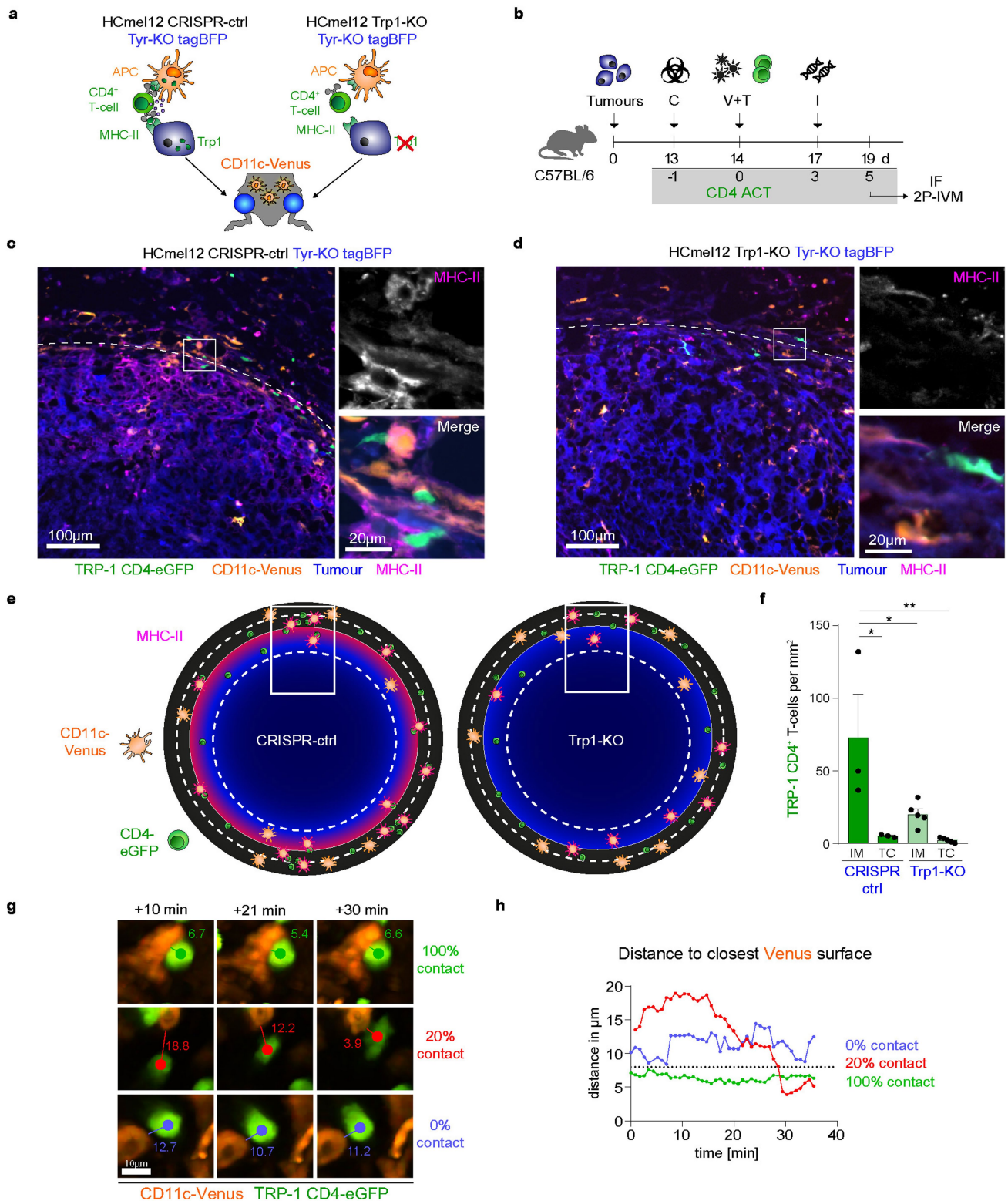
a, Representative flow cytometric histograms for MHC-I and MHC-II expression of indicated melanoma cells in the presence or absence of IFN γ . **b,** Graphical representation of the interaction phenotype of the indicated melanoma cells (left) and experimental treatment protocol (right). **c,** Individual tumour growth curves of mice bearing established melanomas and treated as indicated. **d,** t-SNE heatmaps of multiparametric flow cytometry for HcMel12 melanoma single cell suspensions showing the indicated markers (top) and corresponding annotation (bottom) of TRP-1 CD4+ T-cells (GFP⁺), Pmel-1 CD8+ T-cells (Venus⁺), immature monocytes (CD11b⁺ Ly6C^{hi}), mature monocytes (CD11b⁺ Ly6C^{lo}), mature macrophages (CD11b⁺ F4/80⁺), dendritic cells (CD11b⁺ MHC-II⁺ CD11c⁺ F4/80⁻), endogenous lymphocytes (CD11b⁻ CD11c⁻), and

neutrophils (CD11b⁺ Ly6G⁺). **e,** Quantification of the immune cell composition of HcMel12 CRISPR-ctrl and Jak1-KO tumours treated as indicated. **f,** Recombinant adenovirus Ad-OVA (top) and experimental protocol (bottom) to assess the *in vivo* expansion of adoptively transferred ovalbumin-specific CD8+ and CD4+ T-cells. **g,** Representative flow cytometric contour plots with 0.5×10^6 transferred T-cells and quantitation of OT-I CD8+ and OT-II CD4+ TCRtg T-cell expansion in peripheral blood 7 days after ACT (mean \pm SEM from n = 9 biologically independent samples, ****p < 0.0001 using a two-tailed paired t-test). **h,** Experimental protocol and (i) individual tumour growth curves of mice bearing established HcMel12-OVA Jak1-KO tumours, treated as indicated. Means between groups were statistically compared using a two-tailed paired t-test.



Extended Data Fig. 4 | CD4⁺ effector T-cells show a different spatial distribution and migratory behaviour in tumour tissues when compared to CD8⁺ effector T-cells. a, Macroscopic phenotype and graphical representation for the generation of amelanotic HCmel12 CRISPR-ctrl or Jak1-KO Tyr-KO tagBFP cell lines (top) and experimental treatment protocols (bottom). b, c, Representative fluorescence image for the distributions of Venus+ Pmel-1 CD8⁺ T-cells and eGFP+ TRP-1 CD4⁺ T-cells in indicated HCmel12 variants. d, e, Diagrammatic representation of the Venus+ Pmel-1 CD8⁺ T-cell and eGFP+ TRP-1 CD4⁺ T-cell distribution in a whole tumour cryosection of HCmel12 Tyr-KO CRISPR-ctrl (d) or Jak1-KO (e) melanomas (left) and corresponding quantitation (right) at the invasive margin (IM) and in the tumour centre (TC) (mean \pm SEM for n = 6-7 biologically independent samples; CD4⁺ IM vs CD4⁺ TC **p = 0.0051, CD4⁺ IM vs CD8⁺ IM **p = 0.0035, CD4⁺ TC vs CD8⁺ TC **p = 0.068

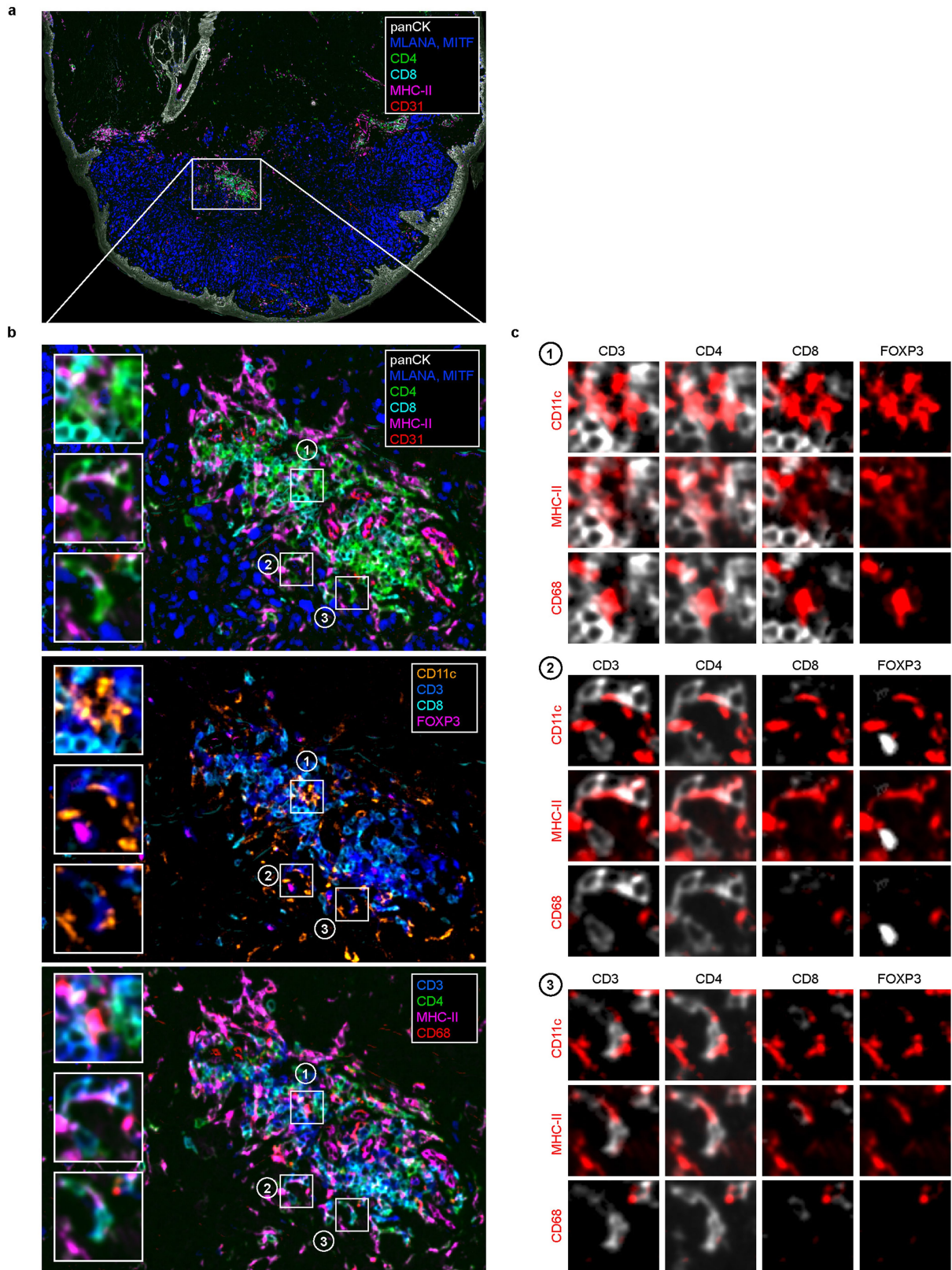
using a one-way ANOVA with Tukey post-hoc). f, Diagrammatic representation and experimental protocol for treatment of HCmel12 Jak1-KO Tyr-KO OVA-tagBFP cells. g, Cell density (mean \pm SEM from 7 biologically independent samples; CD4⁺ IM vs CD8⁺ IM *p = 0.0122, CD4⁺ TC vs CD8⁺ IM *p = 0.0173, CD8⁺ TC vs CD8⁺ IM *p = 0.121 using a one-way ANOVA with Tukey post-hoc) at the IM and in the TC and arrest coefficient (**p = 0.0005, **p = 0.0046 using a Kruskal-Wallis test with Dunn's multiple comparison test) and mean speed (**p = 0.0012, *p = 0.0499 using a Kruskal-Wallis test with Dunn's multiple comparison test) of adoptively transferred of adoptively transferred Venus+ OT-I CD8⁺ and dsRed+ OT-II CD4⁺ T-cells in the stromal (S) and tumoural (T) compartment at the invasive margin (11-794 cells examined from 3 independent experiments; bar indicates the median).



Extended Data Fig. 5 | CD4⁺ effector T-cells cluster with MHC-II-expressing CD11c⁺ immune cells at the invasive margin of mouse melanomas.

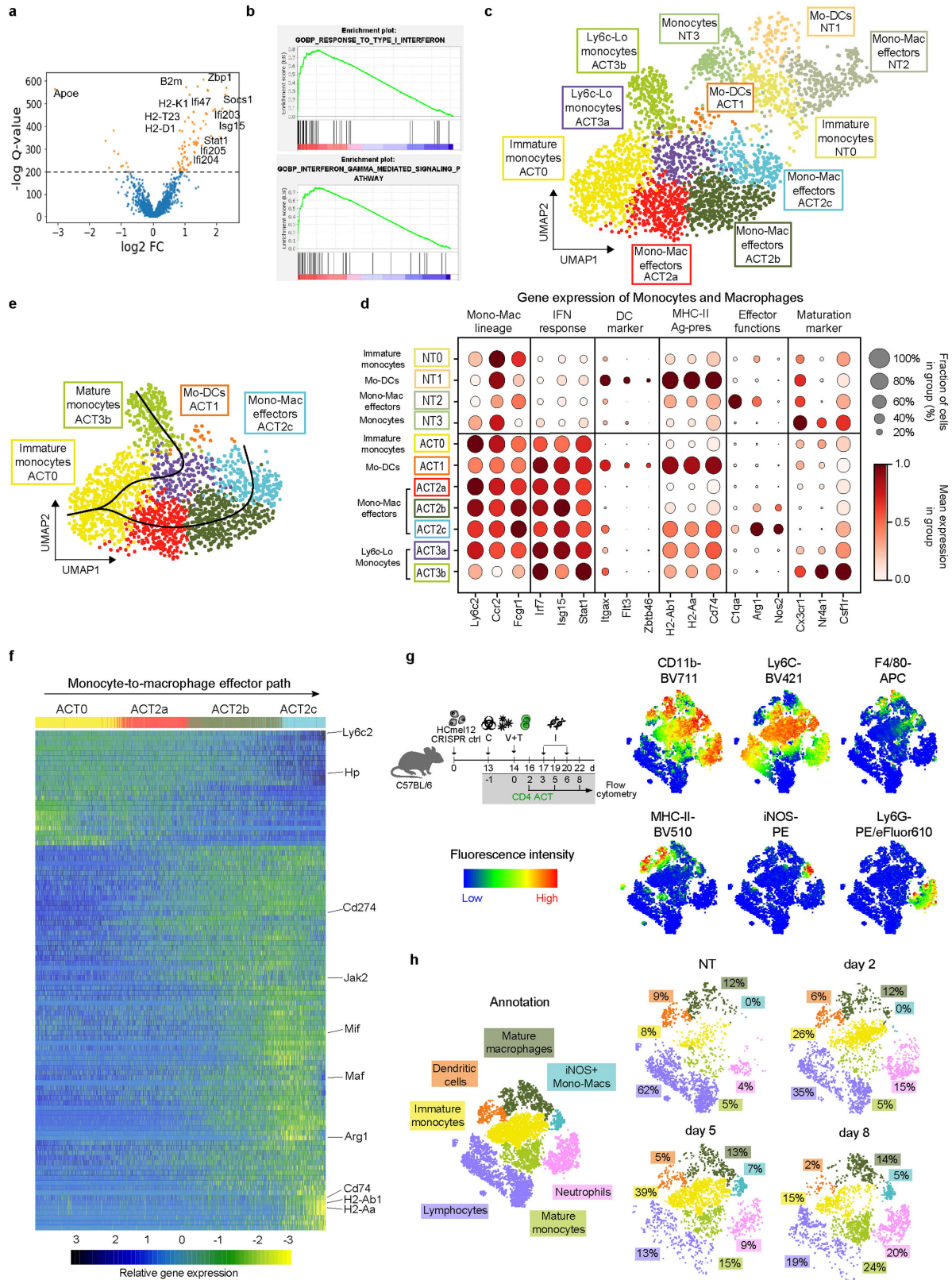
a, Graphical representation of the interaction phenotype of the indicated HCmel12 variants and (b) experimental protocol to study antigen-specific interactions between eGFP⁺ TRP-1 CD4⁺ T-cells and CD11c⁺ cells in CD11c-Venus mice. c,d, Representative immunofluorescence images of MHC-II-stained cryosections from a (c) CRISPR-ctrl and a (d) Trp1-KO melanoma (mean ± SEM from n = 3-5 biologically independent samples). The dashed lines indicate the tumour border. e, Diagrammatic representation of MHC-II expression and

interactions between eGFP⁺ TRP-1 CD4⁺ T-cells and CD11c-Venus antigen-presenting cells in CRISPR-ctrl and Trp1-KO melanomas. f, Density of eGFP⁺ TRP-1 CD4⁺ T-cells at the invasive margin (IM) and in the tumour centre (TC) of indicated tumours (mean ± SEM from n = 3-5 biologically independent samples, **p = 0.0037, CRISPR-ctrl IM vs Trp1-KO IM *p = 0.0267, CRISPR-ctrl IM vs TC *p = 0.0112). Means between groups were statistically compared using a one-way ANOVA with Tukey post-hoc. g,h Intravital 2P-microscopy images of three eGFP⁺ TRP-1 CD4⁺ T-cells and their distance to CD11c-Venus cells over time.



Extended Data Fig. 6 | CD4+ effector T-cells cluster with antigen-presenting dendritic cells and macrophages at the invasive margin of a human melanoma. Multiple iterative labeling by antibody neodeposition (MILAN) of a human melanoma obtained from (Pozniak, J., et al., 2022). An overview (a) over the whole tumour and a selected area of the tumour margin (b) are shown

with multiple label combinations selected from the published panel. Insets (1-3) show exemplary sites of CD4+ T-cell juxtaposition with different myeloid subtypes expressing MHC-II, CD11c, and/or CD68. c, combinatorial overlays of different T-cell markers (white) with myeloid cell markers (red) in the insets (1-3).



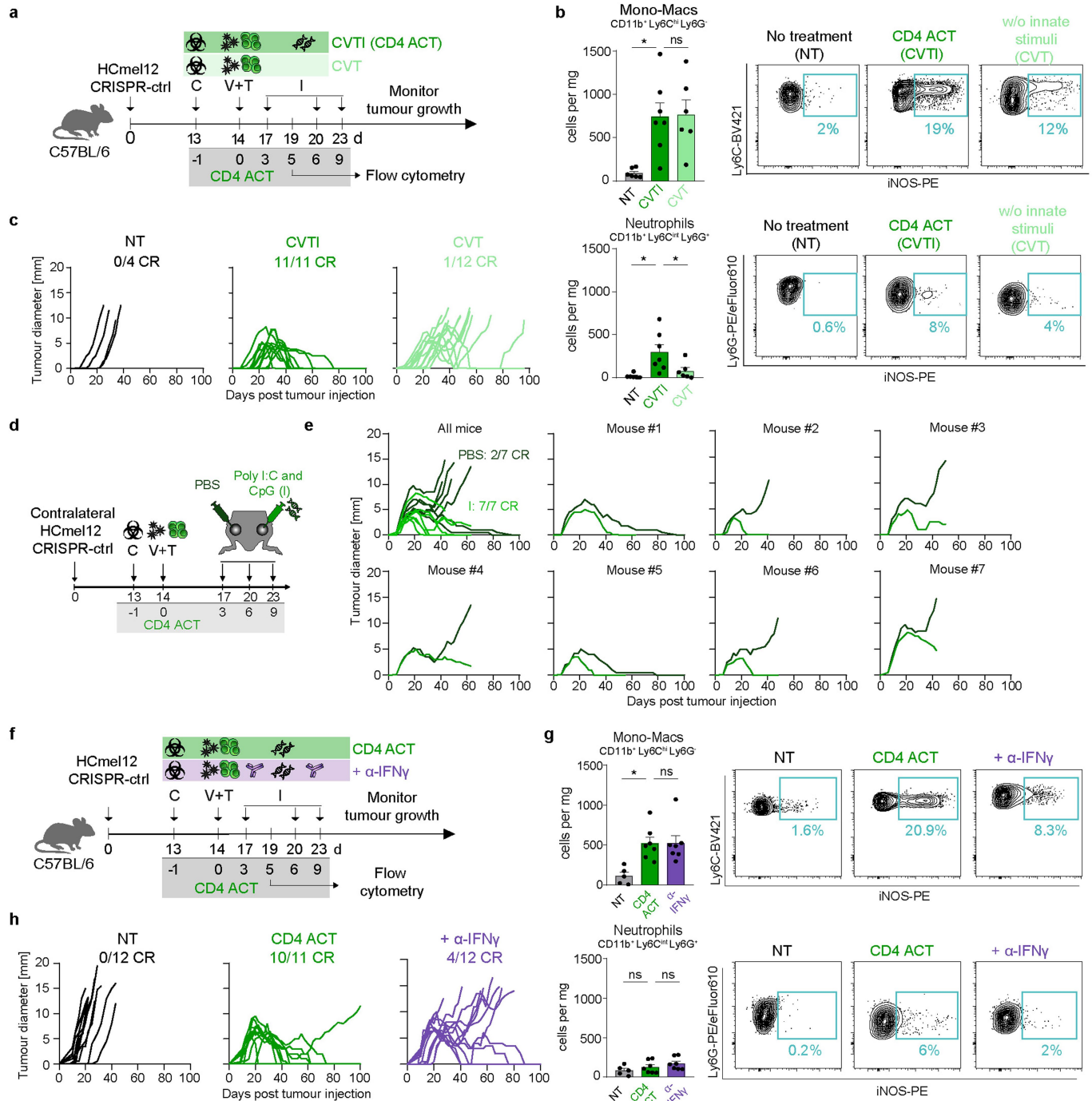
Extended Data Fig. 7 | See next page for caption.

Article

Extended Data Fig. 7 | CD4 ACT therapy predominantly recruits immature monocytes into the tumour microenvironment and drives the acquisition of IFN-activated effector phenotypes.

a, Differentially expressed genes comparing samples from CD4 ACT-treated versus non-treated (NT) mice. Genes with $-\log Q$ -values >200 are shown in orange. b, Gene set enrichment analysis for the "GOBP_RESPONSE_TO_TYPE_I_INTERFERON" (top) and "GOBP_INTERFERON-GAMMA_MEDIATED_SIGNALING_PATHWAY" (bottom) gene sets. c, UMAP plots with Leiden clusters for monocytes and macrophages of CD4 ACT treated tumours. d, Corresponding expression levels and expression cell fractions of selected signature genes for the individual Leiden clusters and (e) pseudotime inference using slingshot. f, Heatmap of differentially

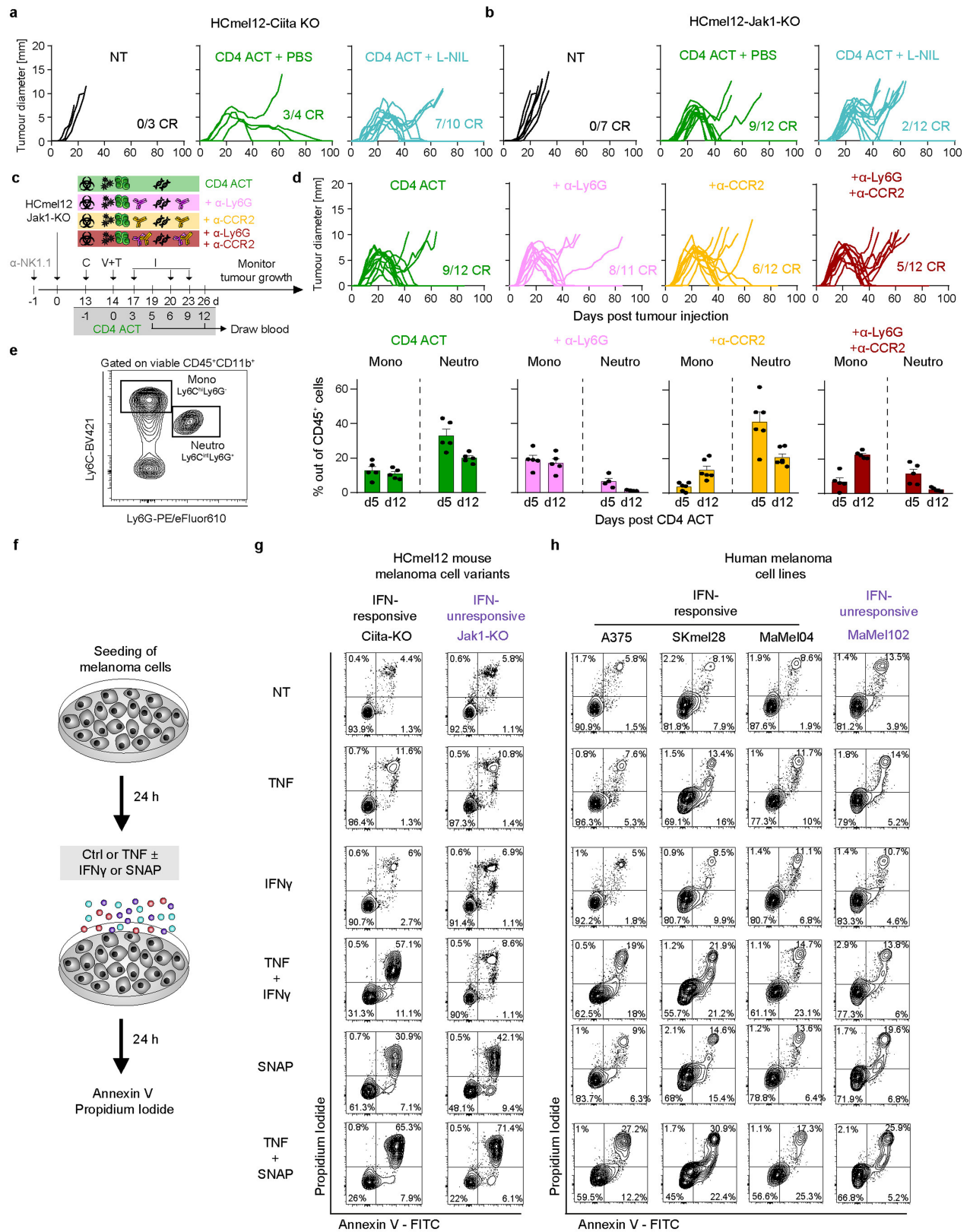
expressed genes along the pseudotime trajectory of the indicated Leiden clusters representing the monocyte-macrophage (mono-mac) effector differentiation path. g, Experimental protocol (left), and t-SNE heatmaps of multiparametric flow cytometry for HCml12 melanoma single cell suspensions showing the indicated markers (right). h, Left: Corresponding annotation of immune of immature monocytes (CD11b+ Ly6Chi), mature monocytes (CD11b+ Ly6clo), mature macrophages (CD11b+ F4/80+ iNOS-), iNOS+ mono-macs (CD11b+ Ly6Chi iNOS+), dendritic cells (CD11b+ MHC-II+ CD11c+ F4/80-), endogenous lymphocytes (CD11b- CD11c-), and neutrophils (CD11b+ Ly6G+). Right: Annotated t-SNE plots quantifying the immune cell composition of HCmel12 melanomas at the indicated time points.



Extended Data Fig. 8 | Robust IFN γ -dependent eradication of established melanomas requires local adjuvant innate immune stimulation.

a, Experimental treatment protocol to address the impact of innate stimuli on myeloid cell activation and tumour control. **b**, Cell density (left) and representative contour plots quantifying the relative iNOS expression (right) in Ly6C^{hi} mono-macs (NT vs CVTI **p* = 0.0109) and neutrophils (NT vs CVTI **p* = 0.0114, CVTI vs CVT **p* = 0.0474) in tumours 5 days post-ACT, treated as indicated (mean \pm SEM from *n* = 6-7 biologically independent samples). **c**, Individual tumour growth curves in mice bearing established melanomas and treated as indicated. **d**, Experimental treatment protocol to address the

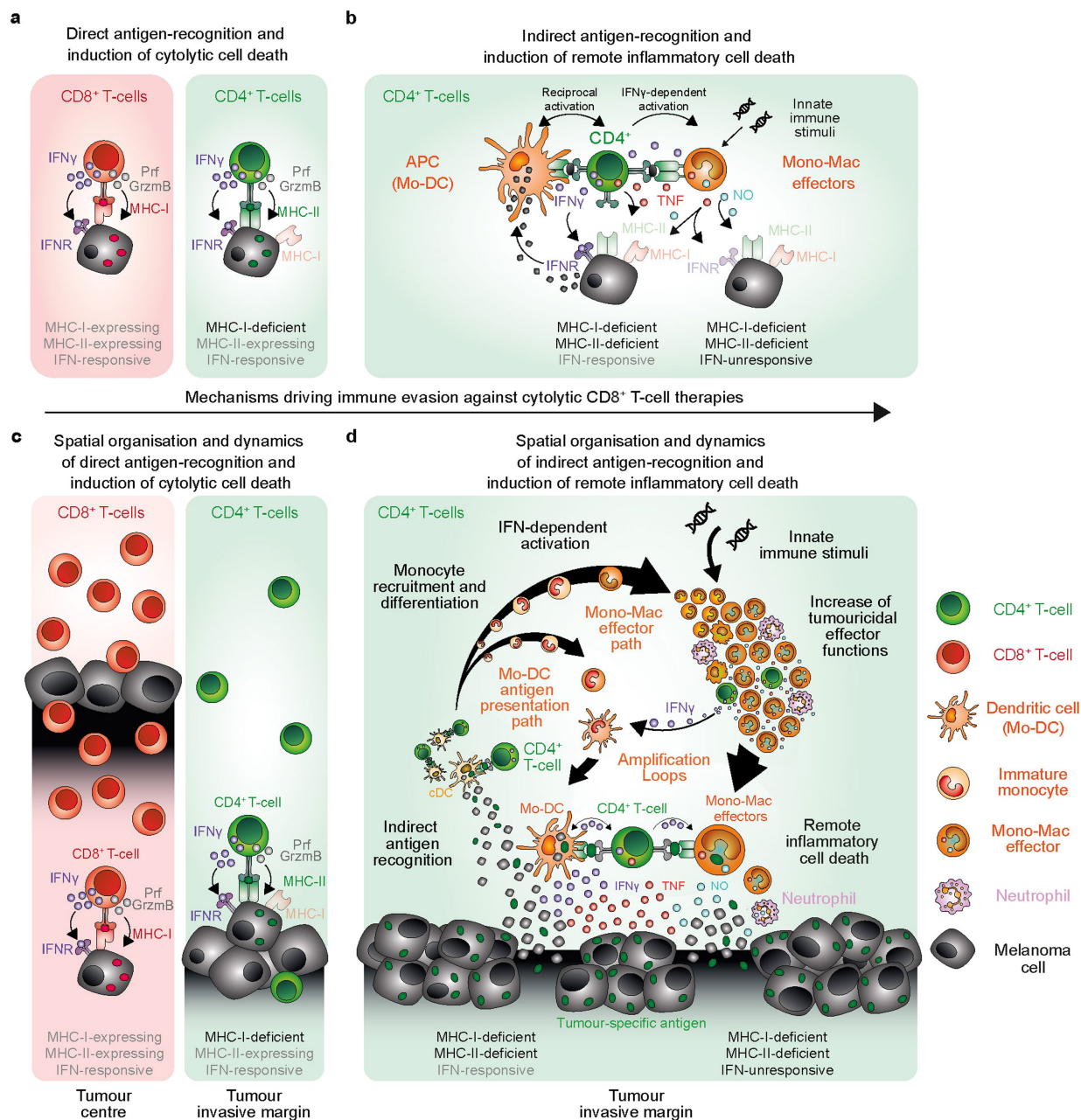
impact of local innate stimuli on tumour control and **(e)** individual growth curves of mice bearing contralateral HCmel12 tumours, treated as indicated. **f**, Experimental treatment protocol to address the impact of IFN γ -blockade. **g**, Cell density (left) and relative iNOS expression (right) in Ly6C^{hi} mono-macs and neutrophils in tumours 5 days post-ACT, treated as indicated (mean \pm SEM from *n* = 6-7 biologically independent samples, **p* = 0.0109). **h**, Individual tumour growth curves of mice bearing established melanomas and treated as indicated. Means between groups were statistically compared using a one-way ANOVA with Tukey post-hoc.



Extended Data Fig. 9 | See next page for caption.

Extended Data Fig. 9 | Chemical iNOS inhibition and antibody-mediated cell depletion of monocytes and neutrophils *in vivo* as well as treatment with the nitric oxide donor SNAP *in vitro* suggest a role for iNOS expressing myeloid cells in the control of established MHC-deficient and IFN-unresponsive melanomas. a,b, Individual tumour growth curves of established HCmel12 Ciita-KO or HCmel12 Jak1-KO melanomas treated as indicated (L-NIL, iNOS-inhibitor). c, Experimental treatment protocol for antibody-mediated depletion of neutrophils and inflammatory monocytes. d, Individual tumour

growth curves of established melanomas treated as indicated. e, Left: Representative gating strategy to evaluate the depletion of monocytes and neutrophils. Right: Flow cytometric percentages of monocytes and neutrophils in the blood 5 and 12 days post-CD4 ACT (mean \pm SEM from 4-6 biologically independent samples). f, Experimental protocol to assess the ability of the inflammatory mediators TNF, IFN γ and the nitric oxide donor SNAP to induce melanoma cell death. g, h, Representative flow cytometric contour plots to assess cell death of mouse and human melanomas treated as indicated.



Extended Data Fig. 10 | Spatial organisation and dynamics of T-cell effector functions in tumour tissues. a, Graphical representation of direct antigen recognition and induction of cytolytic cell death. CD8⁺ and CD4⁺ effector T-cells can recognise their antigens as peptide epitopes presented by MHC-molecules on tumour cell surfaces and initiate direct killing through the release of cytolytic granules. b, Graphical representation of indirect antigen recognition and remote induction of inflammatory cell death. CD4⁺ effector T-cells also efficiently recognise tumour antigen on the surface of antigen-presenting cells (APC) including monocyte-derived dendritic cells (Mo-DC) and engage tumouricidal effector cells of the monocyte-macrophage lineage (Mono-Mac effectors) to initiate indirect cell death through the release of pro-inflammatory mediators. c, Spatial organisation and dynamics of direct induction of cytolytic cell death. CD8⁺ effector T-cells briskly infiltrate tumour tissues, where they directly interact with tumour cells (left), while CD4⁺ effector T-cells directly interact with tumour cells mainly near the invasive margin (right). d, Spatial organisation and dynamics of remote induction of inflammatory cell death. CD4⁺ effector T-cells cluster locally at the tumour invasive margin, where they

indirectly recognise tumour antigen phagocytosed, processed and presented by dendritic cells. Activated CD4⁺ T-cells secrete IFN γ leading to the recruitment and activation of monocytes into the tumour tissue. Recruited monocytes phenotypically develop along differentiations path towards IFN-activated antigen-presenting (monocyte-derived dendritic cells, Mo-DCs) and tumouricidal effector phenotypes (monocyte-macrophage effector cells, Mono-Mac effectors). Mo-DCs additionally activate CD4⁺ T-cells and amplify monocyte recruitment, activation and differentiation. Innate immune stimulation promotes the Th1-directed differentiation of CD4⁺ T-cells and increases the tumouricidal functions of Mono-Mac effectors. CD4⁺ T-cell-derived IFN γ sensitises IFN-responsive melanoma cells for TNF-induced cell death. Myeloid cell-derived nitric oxide (NO) contributes to inflammatory cell death of IFN-unresponsive melanoma cells. Taken together, the induction of remote inflammatory cell death by CD4⁺ T-cells and tumouricidal myeloid cells eradicate IFN-responsive as well as IFN-unresponsive, MHC-deficient tumours that evade direct recognition and cytolytic killing.

Reporting Summary

Nature Portfolio wishes to improve the reproducibility of the work that we publish. This form provides structure for consistency and transparency in reporting. For further information on Nature Portfolio policies, see our [Editorial Policies](#) and the [Editorial Policy Checklist](#).

Statistics

For all statistical analyses, confirm that the following items are present in the figure legend, table legend, main text, or Methods section.

n/a Confirmed

- The exact sample size (n) for each experimental group/condition, given as a discrete number and unit of measurement
- A statement on whether measurements were taken from distinct samples or whether the same sample was measured repeatedly
- The statistical test(s) used AND whether they are one- or two-sided
Only common tests should be described solely by name; describe more complex techniques in the Methods section.
- A description of all covariates tested
- A description of any assumptions or corrections, such as tests of normality and adjustment for multiple comparisons
- A full description of the statistical parameters including central tendency (e.g. means) or other basic estimates (e.g. regression coefficient) AND variation (e.g. standard deviation) or associated estimates of uncertainty (e.g. confidence intervals)
- For null hypothesis testing, the test statistic (e.g. F , t , r) with confidence intervals, effect sizes, degrees of freedom and P value noted
Give P values as exact values whenever suitable.
- For Bayesian analysis, information on the choice of priors and Markov chain Monte Carlo settings
- For hierarchical and complex designs, identification of the appropriate level for tests and full reporting of outcomes
- Estimates of effect sizes (e.g. Cohen's d , Pearson's r), indicating how they were calculated

Our web collection on [statistics for biologists](#) contains articles on many of the points above.

Software and code

Policy information about [availability of computer code](#)

Data collection

Data analysis

Python (version 3.9.9)
 anndata (version 0.7.6)
 anndata2ri (version 1.0.6)
 attrs (version 21.2.0)
 backcall (version 0.2.0)
 certifi (version 2020.12.5)
 cffi (version 1.14.5)
 chardet (version 4.0.0)
 CITE-seq-Count (version 1.4.4)
 cmake (version 3.22.0)
 cutadapt (version 3.5)
 cycler (version 0.10.0)
 Cython (version 0.29.24)
 decorator (version 4.4.2)
 get-version (version 2.2)
 gprofiler-official (version 1.0.0)
 h5py (version 3.2.1)
 idna (version 2.10)
 iniconfig (version 1.1.1)

ipykernel (version 5.5.4)
ipython (version 7.23.1)
ipython-genutils (version 0.2.0)
jedi (version 0.18.0)
Jinja2 (version 2.11.3)
joblib (version 1.0.1)
jupyter-client (version 6.1.12)
jupyter-core (version 4.7.1)
kiwisolver (version 1.3.1)
legacy-api-wrap (version 1.2)
llvmlite (version 0.36.0)
MarkupSafe (version 1.1.1)
matplotlib (version 3.4.2)
matplotlib-inline (version 0.1.2)
natsort (version 7.1.1)
networkx (version 2.5.1)
numba (version 0.53.1)
numexpr (version 2.7.3)
numpy (version 1.21.4)
openpyxl (version 3.0.9)
packaging (version 20.9)
pandas (version 1.2.4)
parso (version 0.8.2)
patsy (version 0.5.1)
pexpect (version 4.8.0)
pickleshare (version 0.7.5)
Pillow (version 8.2.0)
pluggy (version 0.13.1)
prompt-toolkit (version 3.0.18)
ptyprocess (version 0.7.0)
py (version 1.10.0)
pycparser (version 2.20)
Pygments (version 2.9.0)
pynndescent (version 0.5.2)
pyparsing (version 2.4.7)
python-dateutil (version 2.8.1)
pytz (version 2021.1)
pyxlsb (version 1.0.9)
pyzmq (version 22.0.3)
requests (version 2.25.1)
rpy2 (version 3.4.2)
scanpy (version 1.7.2)
scikit-learn (version 0.24.2)
scipy (version 1.6.3)
scvelo (version 0.2.4)
seaborn (version 0.11.1)
sinfo (version 0.3.4)
six (version 1.16.0)
statsmodels (version 0.12.2)
stdlib-list (version 0.8.0)
tables (version 3.6.1)
threadpoolctl (version 2.1.0)
toml (version 0.10.2)
tornado (version 6.1)
tqdm (version 4.60.0)
traitlets (version 5.0.5)
tzlocal (version 2.1)
umap-learn (version 0.5.1)
urllib3 (version 1.26.4)
wcwidth (version 0.2.5)
xlrd (version 1.2.0)
python-igraph (version 0.9.1)
leidenalg (version 0.8.4)
pytest (version 6.2.3)

R (version 4.0.4)
scrn (version 1.18.7)
MAST (version 1.16.0)
SingleCellExperiment (version 1.12.0)
RcppAnnoy (version 0.0.16)
SummarizedExperiment (version 1.20.0)
Biobase (version 2.50.0)
GenomicRanges (version 1.42.0)
GenomeInfoDb (version 1.26.7)
IRanges (version 2.24.1)
S4Vectors (version 0.28.1)

BiocGenerics (version 0.36.1)
 MatrixGenerics (version 1.2.1)
 matrixStats (version 0.63.0)
 gam (version 1.22)
 foreach (version 1.5.1)
 slingshot (version 1.8.0)
 princurve (version 2.1.6)
 glmnet (version 4.1-6)
 Matrix (version 1.3-2)
 RColorBrewer (version 1.1-3)
 plyr (version 1.8.8)
 ggplot2 (version 3.4.0)

For manuscripts utilizing custom algorithms or software that are central to the research but not yet described in published literature, software must be made available to editors and reviewers. We strongly encourage code deposition in a community repository (e.g. GitHub). See the Nature Portfolio [guidelines for submitting code & software](#) for further information.

Data

Policy information about [availability of data](#)

All manuscripts must include a [data availability statement](#). This statement should provide the following information, where applicable:

- Accession codes, unique identifiers, or web links for publicly available datasets
- A description of any restrictions on data availability
- For clinical datasets or third party data, please ensure that the statement adheres to our [policy](#)

The raw sequencing mouse scRNA-seq data are available at the NCBI GEO under the accession GSE230427 without restrictions. The normalized and logarithmised count matrix used for the subsequent analyses is also available at the NCBI GEO under the accession GSE230427 without restrictions.

Human scRNAseq data used in this study are available at the European Genome-Phenome Archive (EGA) with the identifier EGAS00001006488, available for non-commercial research purposes upon reasonable request and subject to review of a project proposal that will be evaluated by the VIB-UZL Data Access Committee.

Field-specific reporting

Please select the one below that is the best fit for your research. If you are not sure, read the appropriate sections before making your selection.

Life sciences
 Behavioural & social sciences
 Ecological, evolutionary & environmental sciences

For a reference copy of the document with all sections, see [nature.com/documents/nr-reporting-summary-flat.pdf](https://www.nature.com/documents/nr-reporting-summary-flat.pdf)

Life sciences study design

All studies must disclose on these points even when the disclosure is negative.

Sample size	The determination of sample sizes for animal experiments was based on our experience with success of tumour engraftment and efficacy of therapeutic intervention in order to adhere to the 3R guidelines of the local Ethics Committee of the Office for Veterinary Affairs. Tumour treatment experiments involved 4-6 mice per group and were performed at least twice. Analyses of tumour immune cell infiltrates and intravital microscopy experiments involved a minimum of 3 mice per group. This yielded consistently reproducible and statistically significant results. Similarly, group sizes for in vitro experiments were determined based on prior knowledge of variation.
Data exclusions	No data was excluded from analysis.
Replication	Experiments were reliably reproduced and the number of experiments performed stated in methods and legends. Culminated and pooled data are shown where possible. Where representative data is shown, relevant experiments were repeated successfully at least twice with the exact number of repeats indicated in each case. Most experiments were repeated at least twice if not three or more times to verify that experimental findings were reproducible.
Randomization	For in vivo tumour treatment experiments, mice were randomized into different groups when the tumours reached between 3-5 mm in diameter.
Blinding	Blinding was not performed in this study. The experimental observations presented would be consistent irrespective of blinding and therefore blinding was not relevant in this study.

Reporting for specific materials, systems and methods

We require information from authors about some types of materials, experimental systems and methods used in many studies. Here, indicate whether each material, system or method listed is relevant to your study. If you are not sure if a list item applies to your research, read the appropriate section before selecting a response.

Materials & experimental systems

n/a	Involved in the study
<input checked="" type="checkbox"/>	<input checked="" type="checkbox"/> Antibodies
<input checked="" type="checkbox"/>	<input checked="" type="checkbox"/> Eukaryotic cell lines
<input checked="" type="checkbox"/>	<input type="checkbox"/> Palaeontology and archaeology
<input type="checkbox"/>	<input checked="" type="checkbox"/> Animals and other organisms
<input type="checkbox"/>	<input checked="" type="checkbox"/> Human research participants
<input checked="" type="checkbox"/>	<input type="checkbox"/> Clinical data
<input checked="" type="checkbox"/>	<input type="checkbox"/> Dual use research of concern

Methods

n/a	Involved in the study
<input checked="" type="checkbox"/>	<input type="checkbox"/> ChIP-seq
<input type="checkbox"/>	<input checked="" type="checkbox"/> Flow cytometry
<input checked="" type="checkbox"/>	<input type="checkbox"/> MRI-based neuroimaging

Antibodies

Antibodies used

MOUSE

Flow cytometry (Antibody, Supplier, Clone, Colour (Catalogue #) Dilution, Lot No.)

Anti-mouse CD45, Biolegend, 30-F11, APC Fire 750 (Cat #103154) 1:1600, B226658
 Anti-mouse CD11c, Biolegend, N418, APC (Cat #117310) 1:200, B206713
 Anti-mouse F4/80, Thermo Fisher, BM8, PE (Cat #12-4801-82) 1:300, 4299805
 Anti-mouse CD11b, Biolegend, M1/70, BV711 (Cat #101242) 1:200, B379696
 Anti-mouse Ly6C, Biolegend, HK1.4, PE-Cy7 (Cat #128018) 1:2000, B200606
 Anti-mouse CD45R (B220), Biolegend, RA3-682, PE (Cat #103208) 1:1000, B224683
 Anti-mouse CD3e, Biolegend, 17A2, BV421 (Cat #100228) 1:500, B295089
 Anti-mouse CD4, BD Biosciences, RM4-5, BV605 (Cat #563151) 1:500, 8039838
 Anti-mouse NK1.1, Biolegend, PK136, APC (Cat #108710) 1:400, B191787
 Anti-mouse CD45, BD Biosciences, 30-F11, FITC (Cat # 553079) 1:1000, 0030912
 Anti-mouse F4/80, Biolegend, BM8, APC (Cat #123116) 1:200, B205476
 Anti-mouse Ly6C, Biolegend, HK1.4, BV421 (Cat #128031) 1:800, B284703
 Anti-mouse iNOS, Thermo Fisher, CXNFT, PE (Cat #12-5920-80) 1:300, 2283975
 Anti-mouse I-A/I-E, Biolegend, M5/114.15.2, BV510 (Cat #107635) 1:800, B336985
 Anti-mouse CD45, Biolegend, 30-F11, BV711 (Cat #103147) 1:200, B339309
 Anti-mouse CD11c, Biolegend, N418, APC Fire 750 (Cat #117352) 1:100, B367888
 Anti-mouse Siglec H, Biolegend, 551, FITC (Cat #129603) 1:400, B292161
 Anti-mouse CD4, ThermoFisher GK1.5, PE (Cat #12-0041-82) 1:1600, E01010-1635
 Anti-mouse CD11b, Biolegend, M1/70, PE-Cy7 (Cat #101216) 1:2000, B203625
 Anti-mouse Ly6G, BD Biosciences, 1A8, PE (Cat #551461) 1:800, 4246573
 Anti-mouse CD3e, Biolegend, 145-2C11, BV711 (Cat #100349) 1:100, B275433
 Anti-mouse CD8 α , Biolegend, 53-6.7, APC Fire 750 (Cat #100766) 1:1600, B247625
 Anti-mouse H2-Kb, Biolegend, AF6-88.5, PE (Cat #116508) 1:500, B179854
 Anti-mouse I-A/I-E, Biolegend, M5/114.15.2, APC (Cat #107614) 1:2000, B191785
 Anti-mouse CD3e, Biolegend, 145-2C11, FITC (Cat #100306) 1:100, B241616
 Anti-mouse CD335 (Nkp46), Biolegend, 29A1.4, APC (Cat #137608) 1:100, B375108
 Anti-mouse CD8 α , BD Biosciences, 53-6.7, PE (Cat #137608) 1:800, 5047674
 Anti-mouse V β 14 T cell receptor, BD Biosciences, 14-2, FITC (Cat # 553258) 1:2000, 6259505
 Anti-mouse T-bet, Biolegend, 4B10, PeCy7, (Cat# 644824) 1:200, B214294
 Anti-mouse Foxp3, Biolegend, MF-14, Alexa Fluor 647 (Cat# 126408) 1:100, B358685
 Anti-mouse CD16/32, BioLegend, 93 (Cat # 101320) 1:300, B266362

Western blot (Antibody, Supplier, Clone (Catalogue #) Dilution, Lot No.)

Anti-mouse β -Actin (C4), Santa Cruz Biotechnology (Cat #sc-47778 HRP) 200 μ g/ml, L3112
 Anti-mouse TRP1 (M-19), Santa Cruz Biotechnology, Goat polyclonal (Cat #sc-10448) 1:1000, 0593-100808W5
 Anti-goat HRP, Santa Cruz Biotechnology (Cat #sc-2354) 1:2000, A0319

In vivo depletion (Antibody, Supplier, Clone (Catalogue #) Lot No.)

Anti-mouse MHC-II, BioXCell, Y3P (Cat #BE0178), 796422M2
 Anti-mouse NK1.1, BioXCell, PK136 (Cat #BE0036), 796521N1
 Anti-mouse CD8, BioXCell, 2.43 (Cat #BE0061), 666418M1
 Anti-mouse Ly6G, BioXCell, 1A8 (Cat #BE0075-1), 673218J1
 Anti-mouse IFN γ , BioXCell, XMG1.2 (Cat #BE0055), 791321M1
 Anti-mouse CCR2, Matthias Mack, MC21

Single cell RNA sequencing hashtags (Antibody, Supplier, Clone (Catalogue #) Dilution, Lot No.)

TotalSeq™-B0301 anti-mouse Hashtag 1, Biolegend, M1/42; 30-F11, (Cat # 155831), 1:300, B324862
 TotalSeq™-B0302 anti-mouse Hashtag 2, Biolegend, M1/42; 30-F11, (Cat # 155833), 1:300, B329819
 TotalSeq™-B0303 anti-mouse Hashtag 3, Biolegend, M1/42; 30-F11, (Cat # 155835), 1:300, B324863
 TotalSeq™-B0304 anti-mouse Hashtag 4, Biolegend, M1/42; 30-F11, (Cat # 155837), 1:300, B327527
 TotalSeq™-B0305 anti-mouse Hashtag 5, Biolegend, M1/42; 30-F11, (Cat # 155839), 1:300, B318761

TotalSeq™-B0306 anti-mouse Hashtag 6, Biolegend, M1/42; 30-F11, (Cat # 155841), 1:300, B319551
 TotalSeq™-B0307 anti-mouse Hashtag 7, Biolegend, M1/42; 30-F11, (Cat # 155843), 1:300, B326966
 TotalSeq™-B0308 anti-mouse Hashtag 8, Biolegend, M1/42; 30-F11, (Cat # 155845), 1:300, B318319
 TotalSeq™-B0309 anti-mouse Hashtag 9, Biolegend, M1/42; 30-F11, (Cat # 155847), 1:300, B326544
 TotalSeq™-B03010 anti-mouse Hashtag 10, Biolegend, M1/42; 30-F11, (Cat # 155849), 1:300, B318317

Immunofluorescence (Antibody, Supplier, Colour, (Catalogue #) Dilution, Lot No.)

Rat anti-mouse I-A/I-E, BD Bioscience, M5/114.15.2, Purified (Cat #556999) 1:50, 6104526
 Donkey anti-rat IgG (H+L), Jackson ImmunoResearch, Alexa Fluor 594 (Cat #712-585-150) 1:100, 126246

HUMAN

Immunohistochemistry (Antibody, Supplier, Clone (Catalogue #) Dilution, Lot No.)

Anti-human MHC-I (HLA-Class 1 ABC), Abcam, EMR8-5 (Cat #ab70328), 1:100, 20064861
 Anti-human MHC-II (HLA-DP,DQ,DR), Abcam, CR3/43 (Cat #ab7856), 1:200, 12253498
 Anti-human CD8, VENTANA, SP57 (Cat #05937248001), Undiluted, J16713
 Anti-human MART-1 (MelanA), VENTANA, A103, (Cat #05278350001), Undiluted, J29957
 Anti-human gp100, VENTANA, HMB45, (Cat #05479282001), Undiluted J27017
 Anti-human S100, VENTANA, 4C4.9, (Cat #05278104001), Undiluted, J27878
 Anti-human SOX10, Vitro Master Diagnostica, EP268 (Cat #MAD-000656QD-12), Undiluted, 065600465

MILAN (Antibody, Supplier, Clone (Catalogue #) Dilution, Lot No.)

Anti-human CD3, Sigma Aldrich, polyclonal (Cat# C7930) 1 µg/mL, WB3189161
 Anti-human panCK, Santa Cruz Biotechnology, LP5K (Cat# sc-53264) 1 µg/mL, 11246817
 Anti-human CD4, Abcam, EPR6855, (Cat# ab133616) 1:200, GR3276764-17
 Anti-human Foxp3, Abcam, 236A/E7, (Cat# ab20034) 1 µg/mL, GR3409148-10
 Anti-human MHC-II, Novus Biologicals, SPM288 (Cat# NBP2-45312) 1 µg/mL, G0615
 Anti-human CD68, Thermo Fischer Scientific, PGM1 (Cat# MA5-12407) 1:200, VB2949567
 Anti-human Melan-A, Novus Biologicals, A19-P (Cat# NBP1-30151) 1:500, 41343161
 Anti-human CD31, Santa Cruz Biotechnology, JC70 (Cat# sc-53411) 1 µg/mL, D1913
 Anti-human CD11c, Santa Cruz, ITGAX (Cat# SC-46677), 1 µg/mL, H2416
 Anti-human MITF, Dako, DS (Cat#M3621), 1 µg/mL, 10051273

Validation

All antibodies were obtained from commercial vendors and specificity was based on descriptions and information provided in corresponding data sheets provided by the manufacturers, and confirmed via in-house antibody titrations.

Validation statement for each antibody is provided on the manufacturer's website:

MOUSE

Flow cytometry

Anti-mouse CD45-APC Fire 750
<https://www.biolegend.com/nl-be/products/apc-fire-750-anti-mouse-cd45-antibody-13049>
 Anti-mouse CD11c-APC
<https://www.biolegend.com/de-at/products/apc-anti-mouse-cd11c-antibody-1813>
 Anti-mouse F4/80-PE
<https://www.thermofisher.com/antibody/product/F4-80-Antibody-clone-BM8-Monoclonal/12-4801-82>
 Anti-mouse CD11b-BV711
<https://www.biolegend.com/en-us/products/brilliant-violet-711-anti-mouse-human-cd11b-antibody-7927?GroupID=BLG10552>
 Anti-mouse Ly6C-PeCy7
<https://www.biolegend.com/en-gb/products/pe-cyanine7-anti-mouse-ly-6c-antibody-6063>
 Anti-mouse CD45R, (B220) - PE
<https://www.biolegend.com/de-de/products/pe-anti-mouse-human-cd45r-b220-antibody-447>
 Anti-mouse CD3e -BV421
<https://www.biolegend.com/de-de/products/brilliant-violet-421-anti-mouse-cd3-antibody-7326>
 Anti-mouse CD4-BV605
<https://www.bdbiosciences.com/en-de/products/reagents/flow-cytometry-reagents/research-reagents/single-color-antibodies-ruo/bv605-rat-anti-mouse-cd4.563151>
 Anti-mouse NK1.1-APC
[biolegend.com/en-us/products/apc-anti-mouse-nk-1-1-antibody-427?GroupID=GROUP20](https://www.biolegend.com/en-us/products/apc-anti-mouse-nk-1-1-antibody-427?GroupID=GROUP20)
 Anti-mouse CD45-FITC
<https://www.bdbiosciences.com/zh-cn/products/reagents/flow-cytometry-reagents/research-reagents/single-color-antibodies-ruo/fitc-rat-anti-mouse-cd45.553079>
 Anti-mouse F4/80-APC
<https://www.biolegend.com/en-us/products/apc-anti-mouse-f4-80-antibody-4071?GroupID=BLG5319>
 Anti-mouse Ly6C-BV421
<https://www.biolegend.com/de-de/products/brilliant-violet-421-anti-mouse-ly-6c-antibody-8586>
 Anti-mouse iNOS-PE
<https://www.thermofisher.com/antibody/product/iNOS-Antibody-clone-CXNFT-Monoclonal/12-5920-82>
 Anti-mouse I-A/I-E-BV510
<https://www.biolegend.com/en-us/products/brilliant-violet-510-anti-mouse-i-a-i-e-antibody-7997?GroupID=BLG11931>

Anti-mouse CD45-BV711
<https://www.biolegend.com/nl-nl/products/brilliant-violet-711-anti-mouse-cd45-antibody-10439>
 Anti-mouse CD11c-APC Fire 750
<https://www.biolegend.com/en-us/products/apc-fire-750-anti-mouse-cd11c-antibody-13050?6664>
 Anti-mouse Siglec H- FITC
<https://www.biolegend.com/nl-be/products/fitc-anti-mouse-siglec-h-antibody-5177>
 Anti-mouse CD4-PE
<https://www.thermofisher.com/antibody/product/CD4-Antibody-clone-GK1-5-Monoclonal/12-0041-82>
 Anti-mouse CD11b-PE-Cy7
<https://www.biolegend.com/en-us/products/pe-cyanine7-anti-mouse-human-cd11b-antibody-1921?GroupID=BLG10427>
 Anti-mouse Ly6G-PE
<https://www.bdbiosciences.com/en-eu/products/reagents/flow-cytometry-reagents/research-reagents/single-color-antibodies-ruo/pe-rat-anti-mouse-ly-6g.551461>
 Anti-mouse CD3 ϵ -BV711
<https://www.biolegend.com/fr-fr/products/brilliant-violet-711-anti-mouse-cd3epsilon-antibody-11975>
 Anti-mouse CD8 α -APC Fire 750
<https://www.biolegend.com/de-de/products/apc-fire-750-anti-mouse-cd8a-antibody-13048>
 Anti-mouse H2-Kb-PE
<https://www.biolegend.com/en-us/products/pe-anti-mouse-h-2kb-antibody-1749?GroupID=BLG2539>
 Anti-mouse I-A/I-E-APC
<https://www.biolegend.com/en-us/products/apc-anti-mouse-i-a-i-e-antibody-2488>
 Anti-mouse CD3 ϵ -FITC
<https://www.biolegend.com/en-us/products/fitc-anti-mouse-cd3epsilon-antibody-23>
 Anti-mouse CD335 (NKp46) - APC
<https://www.biolegend.com/de-at/products/apc-anti-mouse-cd335-nkp46-antibody-6676?GroupID=BLG8849>
 Anti-mouse CD8 α -PE
<https://www.bdbiosciences.com/en-de/products/reagents/flow-cytometry-reagents/research-reagents/single-color-antibodies-ruo/pe-rat-anti-mouse-cd8a.553032>
 Anti-mouse V β 14 T cell receptor-FITC
<https://www.bdbiosciences.com/en-eu/products/reagents/flow-cytometry-reagents/research-reagents/single-color-antibodies-ruo/fitc-rat-anti-mouse-v-14-t-cell-receptor.553258>
 Anti-mouse T-bet-PeCy7
<https://www.biolegend.com/en-us/products/pe-cyanine7-anti-t-bet-antibody-8328?GroupID=BLG6433>
 Anti-mouse Foxp3-Alexa Fluor 647
<https://www.biolegend.com/en-us/products/alexa-fluor-647-anti-mouse-foxp3-antibody-4662>
 Anti-mouse CD16/32
<https://www.biolegend.com/nl-be/products/trustain-fcx-anti-mouse-cd16-32-antibody-5683>

Western blot

Anti-mouse TRP1
<https://datasheets.scbt.com/sc-10448.pdf>
 Anti-mouse β -Actin
<https://datasheets.scbt.com/sc-47778.pdf>
 Anti-goat HPR
<https://www.scbt.com/p/mouse-anti-goat-igg-hrp>

In vivo depletion

Anti-mouse MHC-II
<https://bioxcell.com/invivomab-anti-mouse-mhc-class-ii-i-a-be0178>
 Anti-mouse NK1.1
<https://bioxcell.com/invivomab-anti-mouse-nk1-1-be0036>
 Anti-mouse CD8
<https://bioxcell.com/invivomab-anti-mouse-cd8a-be0061>
 Anti-mouse Ly6G
<https://bioxcell.com/invivomab-anti-mouse-ly6g>
 Anti-mouse IFN γ
<https://bioxcell.com/invivomab-anti-mouse-ifng-be0055>
 Anti-mouse CCR2
 Mack et al., 2001 Journal of Immunology

Single cell RNA sequencing hashtags

TotalSeq™-B0301 anti-mouse Hashtag 1
<https://www.biolegend.com/en-us/products/totalseq-b0301-anti-mouse-hashtag-1-antibody-17771>
 TotalSeq™-B0302 anti-mouse Hashtag 2
<https://www.biolegend.com/en-us/products/totalseq-b0302-anti-mouse-hashtag-2-antibody-17772>
 TotalSeq™-B0303 anti-mouse Hashtag 3
<https://www.biolegend.com/en-us/products/totalseq-b0303-anti-mouse-hashtag-3-antibody-17773>
 TotalSeq™-B0304 anti-mouse Hashtag 4
<https://www.biolegend.com/en-us/products/totalseq-b0304-anti-mouse-hashtag-4-antibody-17774>
 TotalSeq™-B0305 anti-mouse Hashtag 5
<https://www.biolegend.com/en-us/products/totalseq-b0305-anti-mouse-hashtag-5-antibody-17775>
 TotalSeq™-B0306 anti-mouse Hashtag 6
<https://www.biolegend.com/en-us/products/totalseq-b0306-anti-mouse-hashtag-6-antibody-17776>
 TotalSeq™-B0307 anti-mouse Hashtag 7

<https://www.biolegend.com/en-us/products/totalseq-b0307-anti-mouse-hashtag-7-antibody-17777>
TotalSeq™-B0308 anti-mouse Hashtag 8
<https://www.biolegend.com/en-us/products/totalseq-b0308-anti-mouse-hashtag-8-antibody-17778>
TotalSeq™-B0309 anti-mouse Hashtag 9
<https://www.biolegend.com/en-us/products/totalseq-b0309-anti-mouse-hashtag-9-antibody-17779>
TotalSeq™-B03010 anti-mouse Hashtag 10
<https://www.biolegend.com/en-us/products/totalseq-b0310-anti-mouse-hashtag-10-antibody-18225>

Immunofluorescence

Rat anti-mouse I-A/I-E-Purified

<https://www.bdbiosciences.com/en-us/products/reagents/flow-cytometry-reagents/research-reagents/single-color-antibodies-ruo/purified-rat-anti-mouse-i-a-i-e.556999>

Donkey anti-rat IgG (H+L)

<https://www.jacksonimmuno.com/catalog/products/712-585-150>

HUMAN

Immunohistochemistry

Anti-MHC-I (HLA-Class 1 ABC)

<https://www.abcam.com/products/primary-antibodies/hla-class-1-abc-antibody-emr8-5-ab70328.html>

Anti-MHC-II (HLA-DP,DQ,DR)

<https://www.abcam.com/products/primary-antibodies/hla-dr--dp--dq-antibody-cr343-ab7856.html>

Anti-human CD8

<https://shop.roche-diagnostics.ch/labor/05937248001>

Anti-human MART-1 (MelanA)

<https://shop.roche-diagnostics.ch/labor/05278350001>

Anti-human gp100

<https://shop.roche-diagnostics.ch/labor/05479282001>

Anti-human S100

<https://shop.roche-diagnostics.ch/labor/05278104001>

Anti-human SOX10

https://www.medac-diagnostika.de/index.php?controller=product&id_product=10566

MILAN

Anti-human CD3

<https://www.sigmaaldrich.com/DE/en/product/sigma/c7930>

Anti-human panCK

<https://www.scbt.com/p/cytokeratin-7-antibody-lp5k>

Anti-human CD8

<https://www.thermofisher.com/antibody/product/CD8-Antibody-clone-SP16-Monoclonal/MA5-16345>

Anti-human CD4

<https://www.abcam.com/products/primary-antibodies/cd4-antibody-epr6855-ab133616.html>

Anti-human Foxp3

<https://www.abcam.com/products/primary-antibodies/foxp3-antibody-236ae7-ab20034.html>

Anti-human MHC-II

https://www.novusbio.com/products/hla-dr-b1-antibody-spm288_nbp2-45312

Anti-human CD68

<https://www.thermofisher.com/antibody/product/CD68-Antibody-clone-PG-M1-Monoclonal/MA5-12407>

Anti-human MLANA

https://www.novusbio.com/products/melan-a-mart-1-antibody-a19-p_nbp1-30151

Anti-human CD31

<https://www.scbt.com/p/pecam-1-antibody-jc70>

Anti-human CD11c

<https://www.scbt.com/p/integrin-alpha-x-antibody-b-6>

Anti-human MITF

[https://www.agilent.com/en/product/immunohistochemistry/antibodies-controls/primary-antibodies/mitf-\(concentrate\)-76592#productdetails](https://www.agilent.com/en/product/immunohistochemistry/antibodies-controls/primary-antibodies/mitf-(concentrate)-76592#productdetails)

Eukaryotic cell lines

Policy information about cell lines

Cell line source(s)

The mouse HcMel12 cell line and all variants were generated in the Tübing Laboratory. The mouse B16 melanoma cell line was purchased from ATCC.

The human melanoma cell lines MaMel04 and MaMel102 were kindly provided by Dirk Schadendorf. The human melanoma cell lines, Skmel28 and A375, and HEK293T cells were purchased from ATCC. The 911 human embryonic retinoblast cell line was obtained from Crucell.

Authentication

B16, Skmel28, A375 and HEK293T cells were originally obtained from ATCC respectively and were therefore authenticated by

Authentication	the manufacturer. Furthermore, all cell lines were subjected to STR fingerprinting analysis. Successful gene knock-out for the CRISPR-variants of HcMel12 were all confirmed on a genomic (next-generation sequencing), on a transcriptomic (q-PCR)/ proteomic (western blot) and functional level. Fluorescence was always confirmed by flow cytometry.
Mycoplasma contamination	Cell lines regularly tested negative for mycoplasma contamination.
Commonly misidentified lines (See ICLAC register)	No commonly misidentified cell lines were used in this study.

Animals and other organisms

Policy information about [studies involving animals](#); [ARRIVE guidelines](#) recommended for reporting animal research

Laboratory animals	Mice were housed in an ambient temperature- and humidity-controlled environment on a 12-hour light/dark cycle to mimic natural conditions. Laboratory mouse (<i>Mus musculus</i>) strains C57BL/6J mice were purchased from Janvier or Charles River. Pmel-1, TRP1, OT-I and OT-II mice were purchased from Jackson Laboratories and bred in Central Animal Laboratory, House 65, University Hospital Magdeburg. Pmel-1-Venus mice were generated by crossing CAG-Venus mice with pmel-1 mice. TRP-1-eGFP mice were generated by crossing B6-eGFP mice into the TRP-1-deficient Rag1-KO background of TRP-1 mice. OT-I-Venus mice were generated by crossing CAG-Venus mice with OT-I mice. OT-II-dsRed were generated by crossing OT-II mice with hCD2-dsRed mice (kindly provided by Cornelia Harlin). Pmel-Venus, TRP1-GFP, OT-I-Venus, OT-II-dsRed and CD11c-Venus mice were bred in Central Animal Laboratory, House 65, University Hospital Magdeburg. All transgenic strains were maintained on a C57BL/6 background. All mice were aged between 8 and 12 weeks of age at the time experiments commenced. All animal experiments were conducted with male mice on the C57BL/6 background under specific pathogen-free conditions in individually ventilated cages according to the institutional and national guidelines for the care and use of laboratory animals.
Wild animals	No wild animals were used in the study.
Field-collected samples	No field collected samples were included in the study.
Ethics oversight	Approval by the Ethics Committee of the Office for Veterinary Affairs of the State of Saxony-Anhalt, Germany (permit license numbers 42502-2-1393 Uni MD, 42502-2-1586 Uni MD, 42502-2-1615 Uni MD and 42502-2-1672 Uni MD) in accordance with legislation of both the European Union (Council Directive 499 2010/63/EU) and the Federal Republic of Germany (according to § 8, Section 1 TierSchG, and TierSchVersV).

Note that full information on the approval of the study protocol must also be provided in the manuscript.

Human research participants

Policy information about [studies involving human research participants](#)

Population characteristics	Melanoma metastases of 12 male and 8 female patients with a median age of 76 years (range 35-88 years) were biopsied in the Department of Dermatology at the University Hospital Magdeburg. Melanoma metastases of 9 male and 11 female patients with a median age of 66 years (range 34-82 years) were biopsied the Department of Oncology at the UZ Leuven.
Recruitment	From the University Hospital Magdeburg, samples from melanoma metastases were collected as part of a non-interventional single-centre study investigating the dynamics of the inflammatory immune cell composition. From UZ Leuven, biopsies from melanoma metastases were collected as part of a non-interventional single-center prospective study investigating transcriptomic changes upon immune checkpoint inhibition (Prospective Serial biopsy collection before and during immune-checkpoint inhibitor therapy in patients with malignant melanoma (SPECIAL). Biopsies were taken from easily accessible sites (skin, subcutis, lymph node).
Ethics oversight	Participants from the University Hospital Magdeburg: Ethical approval for the observational study under the title "Dynamics of inflammatory responses during the initiation and progression of skin cancer"(Study No. 162/20). Participants from UZ Leuven: Ethical approval from the UZ Leuven Medical Ethical Committee.

Note that full information on the approval of the study protocol must also be provided in the manuscript.

Flow Cytometry

Plots

Confirm that:

- The axis labels state the marker and fluorochrome used (e.g. CD4-FITC).
- The axis scales are clearly visible. Include numbers along axes only for bottom left plot of group (a 'group' is an analysis of identical markers).
- All plots are contour plots with outliers or pseudocolor plots.
- A numerical value for number of cells or percentage (with statistics) is provided.

Methodology

Sample preparation

Blood samples were resuspended in red cell lysis buffer and incubated for 15 minutes at room temperature. The samples were then centrifuged at 350g for 5 minutes and the supernatant was discarded. This process was repeated. FC-Blocking was performed by incubation of the samples with anti-CD16/32 (1:300) for 10 minutes at 4°C. After washing the samples, the cells were then stained with antibodies for 15 minutes at 4°C. The samples were subsequently washed and resuspended in FACS buffer prior to analysis.

Tumours, spleens and lymph nodes were homogenised through a 70 µm strainer to generate single cell suspensions. The samples were then centrifuged at 350g for 5 minutes and the supernatant was discarded. The samples were then resuspended in red cell lysis buffer and incubated for 5 minutes at room temperature. The samples were then centrifuged again and the supernatant was discarded prior to FC-Blocking of the samples with anti-CD16/32 (1:300) for 10 minutes at 4°C. After washing the samples, the cells were then stained with antibodies for 15 minutes at 4°C. The samples were subsequently washed and resuspended in FACS buffer prior to analysis.

Instrument

Attune NxT flow cytometer.

Software

Attune NxT for collection and FlowJo v10.8.1 (Treestar) for analysis.

Cell population abundance

To quantify the abundance of immune cell subpopulations in tumour tissues, 2000 cells of interest per biological sample were concatenated to a single FCS file. t-SNE plots were generated in FlowJo using the opt-SNE learning configuration (<https://www.nature.com/articles/s41467-019-13055-y>). The vantage-point tree KNN algorithm and the Barnes-Hut gradient algorithm set to 1000 iterations, 30 perplexity and 840 learning rate.

Gating strategy

Please refer to Supplementary Figure 1.

For blood, Pmel cells were identified using the following gating strategy: FSCH lo/SSCH intermediate (lymphocytes) --> FSCA/FSCWlo (singlet gate) --> +/- CD45+ (lymphocytes) --> CD8+ Venus (transgenic Pmel).

For blood, Trp1 cells were identified using the following gating strategy: FSCH lo/SSCH intermediate (lymphocytes) --> FSCA/FSCWlo (singlet gate) --> +/- CD45+ (lymphocytes) --> CD8+ eGFP+(transgenic Trp1).

For blood, OT.I cells were identified using the following gating strategy: FSCH lo/SSCH intermediate (lymphocytes) --> FSCA/FSCWlo (singlet gate) --> +/- CD45+ (lymphocytes) --> CD8+ Venus+ (transgenic OT.I).

For blood, OT.II cells were identified using the following gating strategy: FSCH lo/SSCH intermediate (lymphocytes) --> FSCA/FSCWlo (singlet gate) --> +/- CD45+ (lymphocytes) --> CD4+ dsRED+ (transgenic OT.II).

To assess cell death, melanoma cells were identified using the following gating strategy: FSCA/SSCA --> FSCA/FSCWlo (singlet gate) --> PI+ Annexin+ (dead cells).

To quantitate MHC expression, melanoma cells were identified using the following gating strategy: FSCA/SSCA --> FSCA/FSCWlo (singlet gate) --> MHC-I hi or MHC-II hi (histogram gate).

To phenotype intratumoural CD4+ T cells in Figure 1: FSCH lo/SSCH intermediate (lymphocytes) --> FSCA/FSCWlo (singlet gate) --> +/- CD45+ (lymphocytes) --> CD3+ CD4+ --> eGFP+ (transferred) --> T-bet+ (Th1), Foxp3+ (Treg).

To quantitate immune subsets in Figure 1 and Extended Data Figure 3, leukocytes were identified using the following gating strategy: FSCA/SSCA --> FSCA/FSCWlo (singlet gate) --> CD45+ 7AAD- (live leukocytes) --> Immature monocytes (CD11b+ Ly6C hi), mature macrophages, (CD11b+ F4/80+), mature monocytes (CD11b+ Ly6C lo), TRP1 CD4 (GFP+), dendritic cells (CD11b+ MHC-II+ CD11c+), endogenous lymphocytes (CD11b- CD11c-), neutrophils (CD11b+ Ly6G+).

To quantitate immune subsets in Figure 1 and Extended Data Figure 5, leukocytes were identified using the following gating strategy: FSCA/SSCA --> FSCA/FSCWlo (singlet gate) --> CD45+ 7AAD- (live leukocytes) --> Immature monocytes (CD11b+ Ly6C hi), mature macrophages (CD11b+ F4/80+), mature monocytes (CD11b+ Ly6C lo), TRP1 CD4 (GFP+), Pmel CD8 (Venus+), dendritic cells (CD11b+ MHC-II+ CD11c+ F4/80-), endogenous lymphocytes (CD11b- CD11c-), neutrophils (CD11b+ Ly6G+).

To quantitate immune subsets in Figure 3 and Extended Data Figure 9, leukocytes were identified using the following gating strategy: FSCA/SSCA --> FSCA/FSCWlo (singlet gate) --> CD45+ 7AAD- (live leukocytes) --> Immature monocytes (CD11b+ Ly6C hi), mature macrophages (CD11b+ F4/80+ iNOS-), iNOS+ mono/macros (CD11b+ Ly6C hi iNOS+) mature monocytes (CD11b+ Ly6C lo), dendritic cells (CD11b+ MHC-II+ CD11c+ F4/80-), endogenous lymphocytes (CD11b- CD11c-), neutrophils (CD11b+ Ly6G+).

To quantitate immune subsets in Extended Data Figure 10, leukocytes were identified using the following gating strategy: FSCA/SSCA --> FSCA/FSCWlo (singlet gate) --> CD45+ 7AAD- (live leukocytes) --> Monocytes (CD11b+ Ly6C hi) and neutrophils (CD11b+ Ly6G+).

Tick this box to confirm that a figure exemplifying the gating strategy is provided in the Supplementary Information.